

Evaluation of the Effect of Mineral Dust Aerosol on the Forecast Skill of Numerical Weather Prediction Models based on Remote Sensing Observations

Der Fakultät für Physik und Geowissenschaften
der Universität Leipzig
eingereichte

T H E S I S

zur Erlangung des akademischen Grades

MASTER OF SCIENCE
Msc.

vorgelegt

von Hannes Jascha Griesche Bsc.
geboren am 13. Juni 1988 in Steinfurt

Gutachterin: Prof. Dr. I. Tegen
Zweitgutachter: Jun.-Prof. Dr. B. Pospichal

Leipzig, am 22. Juli 2016

Table of Contents

1	Introduction	1
2	Effects of Mineral Aerosols on Meteorological Processes	6
2.1	Direct Effect: Changes in net Radiation	6
2.1.1	Direct Radiative Forcing by Saharan Dust and Smoke resulting from burning Biomass	7
2.1.2	Semi-Direct Effect: Absorption of Radiation inside Clouds	8
2.2	Indirect Effects	9
2.2.1	Formation of Cloud Droplets and Ice Crystals	9
2.2.2	Observation of Indirect Effects caused by Mineral Dust	10
2.3	Modeling of the Direct and Indirect Aerosol Effect	13
3	Ground-Based Observation of Cloud Parameters	18
3.1	Light Detection and Ranging (Lidar)	19
3.2	Cloud Radio Detection and Ranging (Cloud Radar)	21
3.3	Microwave Radiometer	22
3.4	Cloud Classification	22
3.5	Retrieval of Cloud Microphysical Properties	24
4	Model Data	30
4.1	Consortium for Small-scale Modeling (COSMO)	30
4.1.1	COSMO-EU	30
4.1.2	COSMO-DE	31
4.2	European Centre for Medium-Range Weather Forecasts — Integrated Forecast System (ECMWF-IFS)	31
5	Methodology	33
5.1	How to Determine the Effect of Mineral Dust Aerosol on the Predictability of Clouds and Cloud Properties by Numerical Weather Prediction Models? . . .	33
5.1.1	Identification of Dust-Laden Episodes: BSC-DREAM8b v2	33
5.1.2	Dust Concentration - Temperature Grid	34
5.1.3	Scaling of Measurements on Model Grid	35

5.1.4 Statistical Analysis	35
6 Dust Outbreak Spring 2014	37
7 Long-term Statistic	44
8 Discussion	52
9 Conclusion and Outlook	57
Bibliography	58
A Case study observations scaled on the COSMO-EU and COSMO-DE grid	67
List of Figures	67
List of Tables	72

Chapter 1

Introduction

The state of the atmosphere and its long- and short-term development play a major role in daily life on earth. Knowledge about the atmospheric state can save lives because it enables warnings to the public about meteorological hazards and supports the required emergency management. It can help to reduce or even prevent economic losses, and can simply inform the citizens. To predict the evolution of the atmospheric state *Abbe* [1901] and *Bjerknes* [1904] proposed more than a century ago to use the laws of physics to forecast the weather. Today this idea is implemented in various numerical weather prediction (NWP) models all over the world. In a recent review *Bauer et al.* [2015] have illustrated the evolution of NWP models and highlighted the fundamental developments in forecast skills. They pointed out that the prediction skills have been increased significantly during the last 40 years, as it is presented in Figure 1.1.

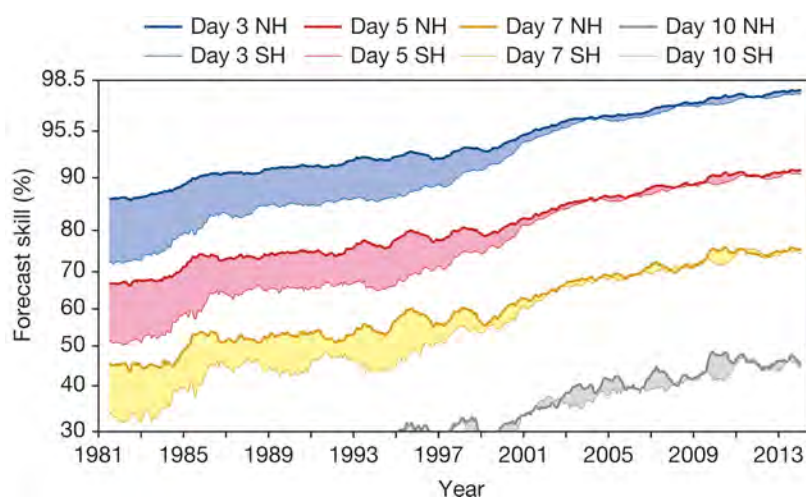


Figure 1.1: Development of the forecast skills of NWP models for the three-, five-, seven-, and ten-day forecasts on the northern hemisphere (NH, thick line) and on the southern hemisphere (SH, thin line) [*Bauer et al.*, 2015].

One major progress in terms of weather prediction was due to the improved parametrization of physical processes [Bauer *et al.*, 2015]. These processes involve radiative, convective, and diffusive effects in the atmosphere and at the atmosphere-earth's surface interface, which remain unresolved numerically. These subgrid-scale processes are partially driven by aerosols, trace gases, and water vapor.

Trace gases like CO_2 , CH_4 or N_2O mainly affect the earth's radiation transfer by enhancing the greenhouse effect [Stocker *et al.*, 2013] and hence are important on a climatological time scale. An accurate knowledge about the amount of water vapor in the atmosphere on the other hand may result in a more precise weather prediction [Grzeschik *et al.*, 2008].

Aerosols influence cloud properties and the radiation transfer and can thus cause rapid adjustments by altering the state of the atmosphere indirectly. Aerosols are solid or liquid particles from different origin and configuration suspended in gas. Examples for their sources are forest fires, combustion processes, sea spray or mineral dust erosion by wind. They interact in various ways with ecosystems on land, in water, and in the air and can be carried over kilometers [Chung and Seinfeld, 2002; Choobari *et al.*, 2014]. A portrait of the global aerosol distribution is shown in Figure 1.2. The shades blue, green, white, and red represent aerosol from sea salt, smoke, sulfate, and dust, respectively.

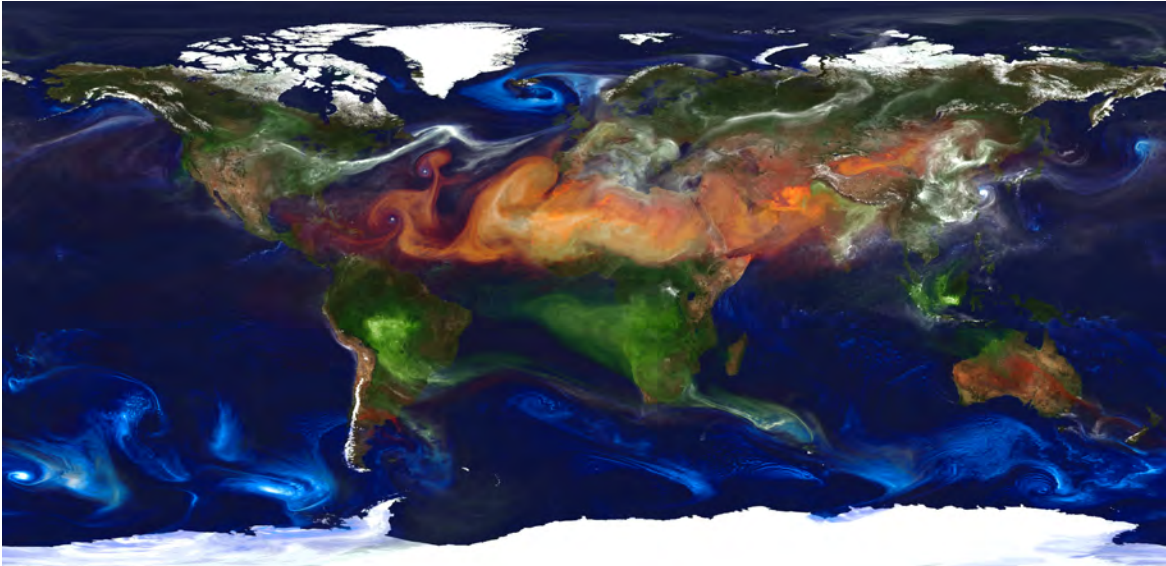


Figure 1.2: Portrait of the global aerosol distribution. Green indicates smoke rising from fires, white sulfate from volcanoes and fossil fuel emissions, blue sea salt inside cyclones, and red is dust erosion [William Putman, 2016].

Mineral dust from arid and semi-arid regions represent the largest amount of aerosol mass and aerosol optical thickness in the atmosphere [Tegen *et al.*, 1997; Textor *et al.*, 2006]. Estimations of the total annual emission ranges from 1000 to 3000 Mt with an average atmospheric burden of 8 to 36 Mt [Zender *et al.*, 2004]. Releasing about 700 Mt per year, the Saharan Desert is considered the world’s largest source of mineral aerosol [Laurent *et al.*, 2008]. Mineral dust provides nutrient matter [Jickells *et al.*, 2005], affects the air quality [Prospero, 1999], and in doing so the human health [Pope *et al.*, 2002]. In addition it influences weather and climate by changing the snow albedo [Painter *et al.*, 2007], altering the net radiation [Li *et al.*, 2004], and affecting cloud properties. Desert dust was identified as a source for ice nucleating particles (INP) both in laboarty studies [Pruppacher and Klett, 2010] and in statistical analyses, as shown, e.g., by Seifert *et al.* [2010]. It can also act as cloud condensation nuclei (CCN) and thus change the clouds’ radiative properties [Twomey, 1977; Twomey *et al.*, 1984]. Due to its various and complex interactions with the atmosphere, mineral dust contributes considerably to the uncertainty in terms of weather prediction and climate modeling [Bangert *et al.*, 2012].

Several studies suggest that including the interaction of mineral dust with radiation and clouds in NWP models has the potential to improve the quality of the forecasts [Pérez *et al.*, 2006b; Bangert *et al.*, 2012]. A recent study pointed out that during an event with a high mineral dust concentration over central Europe in 2008, the forecast error of the German Meteorological Agency Local Model LM was evidently larger than usual [Flentje *et al.*, 2015]. They compared the 0 – 72 h model run for regions with a high dust concentration to regions with a lower concentration before, during, and after the event. The analysis yielded a temperature anomaly of about 1 – 2 °C, while the forecast was degraded by the Saharan dust [Flentje *et al.*, 2015].

The investigation of the effect of Saharan dust on the surface temperatures, as was done by Flentje *et al.* [2015], is one approach to characterize the response of numerical forecast models on the presence of dust. Temperature anomalies however can be considered as the result of the combined effects of Saharan dust on the radiation balance of the atmosphere and on cloud properties. The aim of this work is thus dedicated to the investigation of the effect of Saharan dust on the numerical weather prediction of cloud processes.

This work is based on the assumption that an increase of the NWP errors during dust events is mainly due to the lack of representation of aerosol-cloud interaction in the NWP models. To illustrate in what way mineral dust has a measurable effect on cloud properties and how it influences the prediction accuracy of the NWP models, the model data will be compared to observational data from the Leipzig Aerosol and Cloud Remote Observations System (LACROS) at the Leibniz Institute for Tropospheric Research (TROPOS) in Leipzig [Wandinger, 2012]. The LACROS data as well as the model data will be evaluated by CLOUDNET [Illingworth *et al.*, 2007] algorithms. Cloudnet combines

light detection and ranging (lidar), cloud radio detection and ranging (cloud-radar), and microwave radiometer measurements to characterize clouds and to provide data products like cloud fraction, and liquid and ice water contents. Models that are going to be analyzed are the regional operational weather systems for Europe and Germany of the German weather service model Consortium for Small-scale Modeling (COSMO), COSMO-EU and COSMO-DE, respectively. Additionally the operational global meteorological forecasting model of the European Centre for Medium-Range Weather Forecasts (ECMWF), the Integrated Forecasting System (ECMWF-IFS) will be evaluated.

A theoretical specification about how mineral dust affects the climate system as well as the results of selected studies about these effects are presented in Chapter 2. In Chapter 3 the approach and the structure of Cloudnet are introduced, while in Chapter 4 the model structures of COSMO-EU, COSMO-DE, and ECMWF-IFS are presented. Chapter 5 defines the methodical approach of this work. Part of this Chapter is also a description of the numerical dust forecast model Dust Regional Atmospheric Model (BSC-DREAM8b v2.0) and how it was used to separate dust-laden from dust-free episodes. In Chapter 6 a major dust event over central Europe which took place in spring of 2014 is characterized and its influence on the NWP skills explicitly analyzed. A long-term study for Leipzig of the mineral dust effects on the NWP models COSMO-EU and COSMO-DE is presented in Chapter 7. Finally a discussion is given in Chapter 8 and the conclusion as well as an outlook are given in Chapter 9.

Chapter 2

Effects of Mineral Aerosols on Meteorological Processes

Effects of mineral dust aerosols on the climate system are on the one hand due to absorption and scattering of shortwave and longwave radiation during strong single events as well as in long-term averages [Li *et al.*, 2004], the so-called direct effect. Indirect effects on the other hand result from the nucleus impact of such particles. This results in changes of the optical properties and the persistence of the clouds [McCormick and Ludwig, 1967; Miller and Tegen, 1998]. In addition semi-direct effects are caused by changes in the cloud temperature structure [Hansen *et al.*, 1997; Ackerman *et al.*, 2000].

2.1 Direct Effect: Changes in net Radiation

Absorption and scattering of shortwave and longwave radiation at mineral aerosol particles causes a temperature increase inside the dust layer (Fig. 2.1). While the combination of

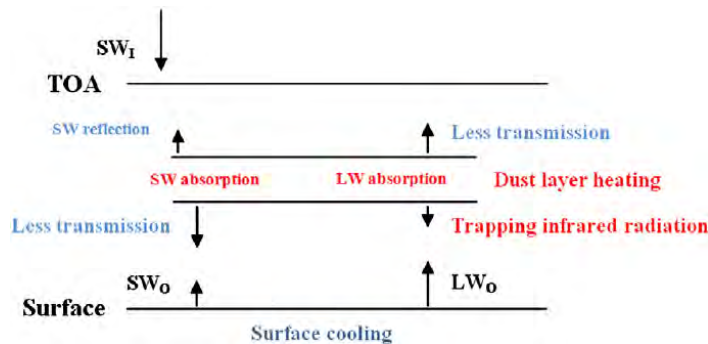


Figure 2.1: Schematic visualization of mineral dust interaction with shortwave (SW) and longwave (LW) radiation during daytime [Choobari *et al.*, 2014]. SW_I indicates the incoming shortwave radiation at the top of atmosphere (TOA), and SW_0 and LW_0 the outgoing radiation at the surface.

absorption and backscattering of shortwave radiation always decreases the incoming solar radiation reaching the surface, the absorption and backscattering of outgoing longwave radiation causes a positive heating rate below the dust layer. The greatest impact on absorption and scattering of shortwave radiation is caused by small particles with a radius in a range of $\sim 0.2 - 2 \mu\text{m}$, while larger particles whose radii are $> 4 \mu\text{m}$ increase the longwave radiative forcing and thus can cause a heating of the surface during the night [Tegen and Lacis, 1996; Miller et al., 2006]. In addition, the residence time of smaller particles in the atmosphere exceeds the one of the larger particles since the latter deposit faster [Seinfeld et al., 1998].

Besides particle size and time of the day, the direct effect depends also on the albedo of the surface below. A dust layer above a bright surface with a high albedo increases the absorption inside the dust layer and thus increases the heating rate in the atmosphere [Choobari et al., 2014]. If the dust layer albedo is larger than the surface albedo then the net radiative forcing is negative [Heintzenberg, 2009].

2.1.1 Direct Radiative Forcing by Saharan Dust and Smoke resulting from burning Biomass

In a study from 2011 the direct radiative forcing caused by Saharan dust and biomass-burning smoke was analyzed by Heinold et al. [2011b]. In doing so they used the multiscale model system COSMO-MUSCAT [Steppeler et al., 2003; Borrego and Incecik, 2004] to simulate the dust distribution over western Africa between the 25th of January 2008 and the 7th of February 2008. On the basis of ground-based and space-borne remote sensing data as well as with local field measurements the model results have been comprehensively evaluated. Figure 2.2 shows the simulated aerosol optical thickness (AOT) at 550 nm wavelength for the 31st of January 2008. On this day the dust layer extended mostly over the western Sahara reaching up to Cape Verde, while smoke mainly had covered the south of western Africa. Areas in blue represent clouds which have not been considered for the calculation of the radiative effect.

The direct radiative effect caused by dust and smoke under clear-sky conditions was analyzed by using two different model settings: one run with neglected aerosol feedback (model run: CTL) and the other with radiative active aerosol particles on the COSMO radiation scheme (model run: RAD). The difference in net radiation of these two runs is given by:

$$\Delta F = (F_{\downarrow} - F_{\uparrow})_{RAD} - (F_{\downarrow} - F_{\uparrow})_{CTL}, \quad (2.1)$$

which is considered the direct dust effect. F_{\downarrow} and F_{\uparrow} identify the downward and upward directed irradiances, respectively. The determined clear-sky net radiative forcing for the 31st of January 2008 is shown in Figure 2.3. The upper row shows the forcing at 12:00 UTC, the lower at 24:00 UTC, left for the top of atmosphere (TOA), center for the surface and

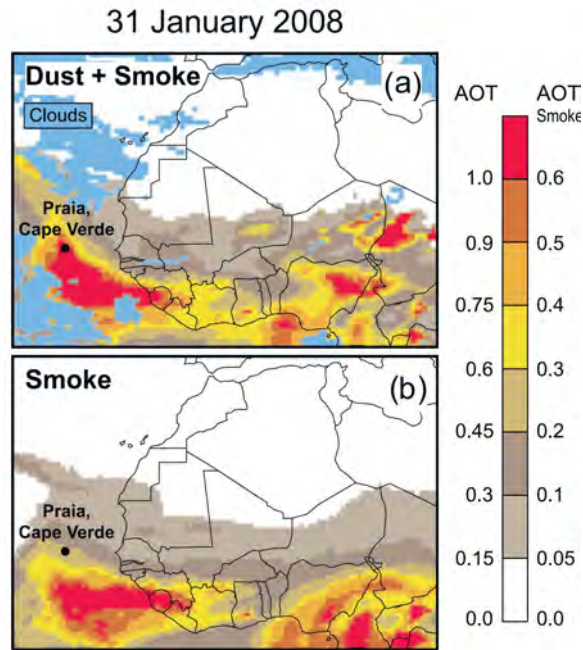


Figure 2.2: Aerosol optical thickness (AOT) from smoke and dust (a) and only smoke (b) on the 31st of January 2008 at 550 nm wavelength [Heinold *et al.*, 2011b].

right for the atmosphere (TOA minus surface). The negative forcing at the TOA above the Atlantic during the day is induced by the smaller albedo from the dust layer, the positive forcing on land is due to the higher reflectivity of the surface compared to the aerosol. This yield a total positive forcing in the atmosphere at noon. The effect during the night can be traced back to terrestrial radiation emissions that has been reduced by the dust layer and thus induced a positive forcing at the surface as well as at the TOA.

2.1.2 Semi-Direct Effect: Absorption of Radiation inside Clouds

The semi-direct effect of mineral dust is caused by absorption due to the aerosols inside clouds. The absorbed radiation heats the cloud and reduces the relative humidity and thus the cloud fraction, the so-called cloud burning effect [Ackerman *et al.*, 2000]. The decreased cloud cover leads to a warming at the surface. This effect is more intense the bigger the aerosol particles are since bigger particles absorb more radiation. Additionally the position of the particles is of importance. If they are located at cloud top they stabilize the air mass and reduce the vertical dimension of the cloud, while their horizontal dimension may be enhanced. If they are located below a cloud the absorbed radiation can cause a convection which results in an increased cloud fraction [Koch and Del Genio, 2010].

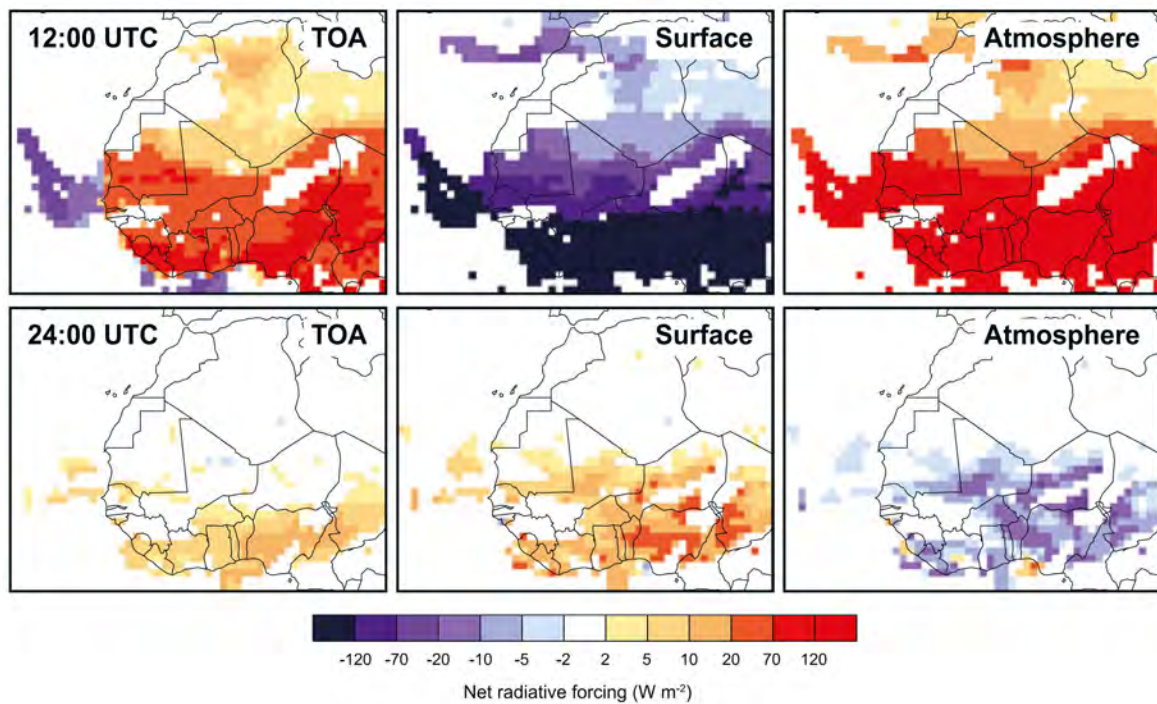


Figure 2.3: Instantaneous net radiative forcing induced by dust and smoke on the 31st of January 2008. The upper row shows the effect at noon (12:00 UTC), the lower at night (24:00 UTC). Left for the top of atmosphere (TOA), center for the surface and right for the atmosphere (TOA minus surface) [Heinold *et al.*, 2011b].

2.2 Indirect Effects

Mineral dust particles can act as seeds for both cloud droplets [Levin *et al.*, 2005] and ice crystals [Hoose and Möhler, 2012] and thus change the cloud nature. Indirect aerosol effects are based upon this nucleus characteristic and their appearance and impact on cloud properties will be discussed within this section.

2.2.1 Formation of Cloud Droplets and Ice Crystals

Drop formation in the atmosphere generally does not occur homogeneously since this process would need a supersaturation of several hundred percent, while it typically remains below 1% [Pruppacher and Klett, 2010]. Also cloud glaciation usually begins at temperatures too high for homogeneous freezing of water [Pruppacher and Klett, 2010]. Thus, in nature drop formation and ice nucleation occurs heterogeneously involving aerosol particles. Therefore mineral dust particles can have a major impact on the size and number of hydrometeors and hence indirect effects on weather and climate. Within this section the principles of heterogeneous cloud droplet and ice crystal formation are outlined first.

Cloud Condensation Nuclei

Soluble particles or the soluble compound of mixed particles can deliquesce into aqueous solution drops and form cloud condensation nuclei (CCN). These CCN can grow when the surrounding relative humidity is high enough [Pruppacher and Klett, 2010]. A theoretical description of the growth of a drop was given by Köhler [1936]. In its simplest algebraic form this theory can be expressed as:

$$s_w = S_w - 1 \approx \frac{a_w}{r} - \frac{b_s}{r^3}, \quad (2.2)$$

where S_w is the saturation ratio of the drop (s_w is the supersaturation), a_w represents the effect of the surface tension given by the Kelvin effect, b_s includes the vapor pressure reduction described by the Raoult effect, and r is the radius. If the ambient supersaturation $s > s_c = \max(s_w)$, or $s < s_c$ and $r < r_c(s_c)$, the drop will grow until $s = s_c$. If $s < s_c$, and $r > r_c$ the droplet will start evaporating [Pruppacher and Klett, 2010].

Ice Nuclei

Supercooled liquid water drops can exist in the atmosphere down to a temperature of about -40°C [Pruppacher and Klett, 2010]. Below -40°C the water will freeze homogeneously. At a temperature above -40°C the freezing process has to be initiated by an aerosol particle, a so called ice nucleating particle (INP). The heterogeneous ice nucleation can occur in various ways. All these processes need a supersaturation with respect to ice, i.e. $\text{RH}_{ice} > 100\%$ with RH_{ice} the relative humidity (RH) with respect to ice.

Four ways of heterogeneous ice nucleation are defined in literature, e.g., Pruppacher and Klett [2010] or Hoose and Möhler [2012]. The first nucleation mechanism describes the direct deposition of water vapor as ice on the INP, the *deposition nucleation*. The second process is the so-called *condensation nucleation*. In this case a supersaturation over water ($\text{RH}_W > 100\%$) at $T < 0^\circ\text{C}$ is necessary. A drop formation triggered by a CCN is initiated and the drop freezes during its condensation stage. If the drop has formed but further cooling is required before the temperature reaches a sufficiently low level the drop will freeze initiated by the immersed INP, the *immersion nucleation*. The fourth mode of heterogeneous ice nucleation is *contact nucleation*. Here, the INP triggers the freezing process by a collision with a supercooled droplet.

2.2.2 Observation of Indirect Effects caused by Mineral Dust

The indirect effects of mineral aerosol have been investigated in several studies and the identified processes are summarized in Figure 2.4. It has been shown for instance that an increase of mineral aerosol concentration at a constant liquid water content (LWC) results in more and thus smaller cloud droplets. The enhanced cloud droplet number concentration

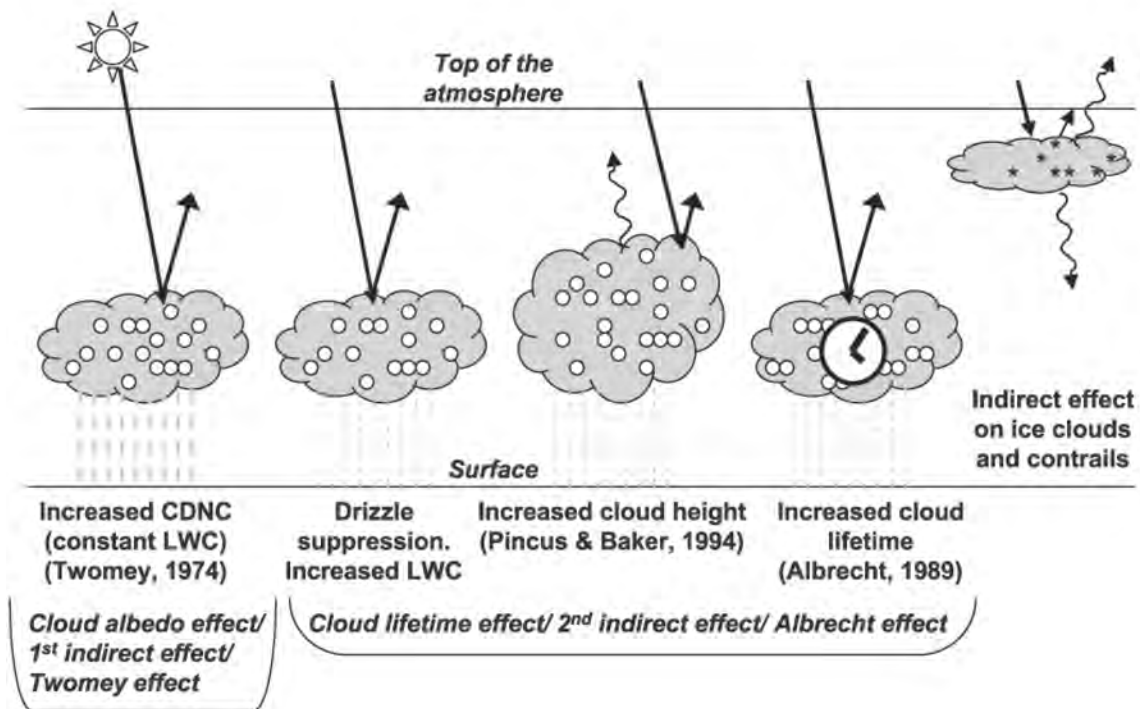


Figure 2.4: Illustration of the indirect aerosol effects. Adapted from *Solomon et al.* [2007].

(at a constant LWC) reduces the optical thickness of a cloud and hence its albedo [*Twomey*, 1974, 1977], the so-called first indirect or cloud albedo effect.

Rosenfeld et al. [2001] combined satellite and aircraft observations and found a higher number of cloud droplets due to desert dust. These cloud droplets are reduced in size due to the limited available water vapor and can thus reduce the precipitation [*Albrecht*, 1989]. Therefore the life time of such clouds and their total reflectivity is increased, the second indirect or cloud lifetime effect, also referred as the Albrecht effect.

Dust-Related Heterogeneous Ice Formation

Mineral dust aerosol can also act as efficient INP [*Sassen et al.*, 2003; *Targino et al.*, 2006; *Teller and Levin*, 2006]. In a field experiment *Sassen et al.* [2003] detected glaciation of mildly supercooled (-5.2 to -8.8°C) altocumulus clouds induced by Saharan dust transported to southern Florida in the United States.

Seifert et al. [2010] investigated the influence of mineral dust on the ice formation in mixed phase clouds over Leipzig. In the time period from February 1997 until June 2008 they compared dust-free cases with dust-laden cases at different cloud top temperatures

(CTT) but apart from that similar meteorological conditions. Especially at a CTT between -10 to -20 °C they found significant differences in the freezing efficiency of mixed phase clouds (see Fig. 2.5). For a dust concentration $c_D \geq 2 \mu\text{g m}^{-3}$ at cloud level and within the above mentioned CTT interval up to 30% more ice clouds were found than for $c_D < 0.001 \mu\text{g m}^{-3}$.

A similar coherence between dust and ice occurrence in midlevel supercooled stratiform clouds (MSSC) was found in a study from *Zhang et al.* [2012]. They analyzed satellite data from a four year interval from the Cloud-Aerosol Lidar with Orthogonal Polarization (CALIOP) mounted on the Cloud-Aerosol Lidar and Infrared Pathfinder Satellite Observations (CALIPSO) satellite and from the Cloud Profiling Radar (CPR) on board of the CloudSat satellite. Using total attenuated backscatter coefficient profiles provided by CALIOP and CPR radar reflectivity factor profiles they created a global distribution of the dust-laden MSSC. The relationship between the radar reflectivity factor Z_e , and particle size and number concentration is described in Section 3.2.

Zhang et al. [2012] identified three different regimes: $\sim 6.3 \cdot 10^5$ dust-laden MSSC profiles, $\sim 3.4 \cdot 10^6$ non-dusty MSSCs, and $\sim 2.6 \cdot 10^6$ MSSCs on the southern hemisphere. The separation between dust-laden, non-dusty, and southern regions is based on the distribution of the dust concentration: since almost every dust-laden case has been found in the dust belt [*Prospero et al.*, 2002] on the northern hemisphere, non-dusty cases on the northern hemisphere might have a background concentration that was difficult to detect for CALIOP. Therefore, the southern hemisphere was included as a region even less burdened by dust.

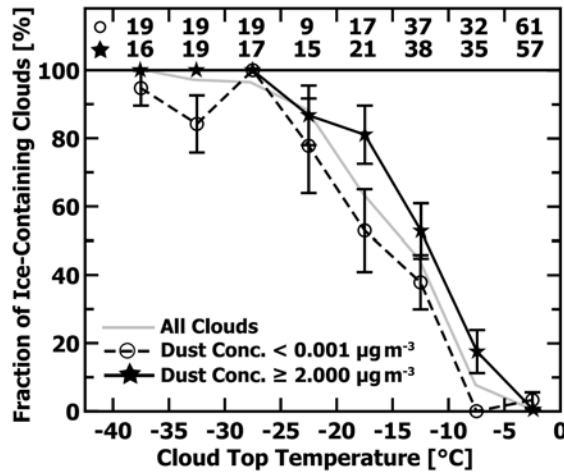


Figure 2.5: Amount of ice in mixed-phase cloud in terms of the cloud top temperature and dust concentration (c_D). The black solid line marks the ratio at a high ($c_D \geq 2 \mu\text{g m}^{-3}$), the dashed line at a small dust concentration ($c_D < 0.001 \mu\text{g m}^{-3}$) and the grey line represents the whole data set [*Seifert et al.*, 2010].

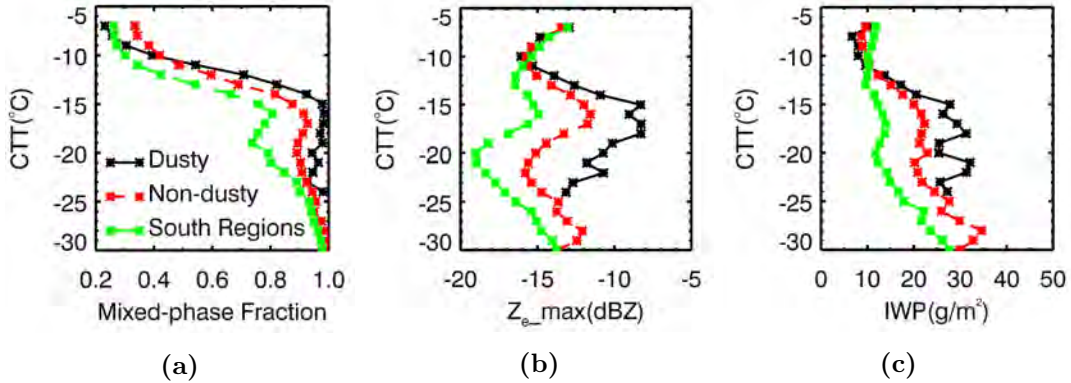


Figure 2.6: Satellite observations of dust effects on mixed-phase clouds from *Zhang et al.* [2012]. For the three different regions (dusty, non-dusty and southern regions) the amount of ice (a), the maximum radar reflectivity factor Z_{e_max} (b) and the ice water path (IWP) (c) in MCCSs in terms of their CTT is represented.

In Figure 2.6a the occurrence of the mean mixed-phase fraction at a given cloud top temperature (CTT) for dusty, non-dusty, and 'South Regions' MSSCs is represented. Figure 2.6b and 2.6c show the same for the mean maximum Z_e (Z_{e_max}) and mean ice water path (IWP), respectively. Analog to *Seifert et al.* [2010] they found greater amounts of ice clouds at $T < -10^\circ\text{C}$ if the dust concentration was enhanced (Fig. 2.6a). In addition, Z_{e_max} and the IWP observed with CloudSat are increased due to the dust burden, especially between -15 and -25°C (Fig. 2.6b and 2.6c).

2.3 Modeling of the Direct and Indirect Aerosol Effect

A study from *Bangert et al.* [2012] analyzed the effect of mineral aerosols on clouds and radiation in Europe during a Saharan dust event in May 2008. They compared four simulations of the online coupled model system COSMO-ART [*Vogel et al.*, 2009] with different settings. A simulation with the index REF neglected dust-radiation as well as dust-cloud interaction. Another simulation called R considered only dust-radiation interaction, simulation C allowed only dust-cloud interaction, and finally simulation CR included dust-radiation as well as dust-cloud interaction. The effect was investigated in two areas: a bigger domain D0 with a coarse resolution extending from Northwest Africa to Western Europe and a smaller domain D1 with a higher resolution covering in large part of Central Europe that was affected by dust (see Fig. 2.7). The simulated time period starts on the 22nd of May 2008 at 00:00 UTC and continues until the 30th of May 2008 at 00:00 UTC.

Figure 2.8a shows the PM_{10} mass concentration measured during this period. The black line represents the measurements at Hohenpeissenberg in southern Germany, the grey line simulated concentrations for the domain D1, and the shadings the simulated concentration for domain D0. The aerosol mass in domain D0 was divided into fractions of dust particles (red shadings) and of all other aerosols (including anthropogenic aerosol particles and sea salt). The decrease of anthropogenic and biogenic particles with increasing dust particle concentration indicates that the aerosol mass of a Saharan dust event over Europe should not simply be added to the typical (continental) aerosol population. In fact it should be simulated explicitly on the basis of anthropogenic and biogenic emissions [Bangert et al., 2012].

Figure 2.8b represents the predicted 2-m temperature (T_{2m}) from the operative NWP model of the German national meteorological service COSMO compared to the observations for a small area in Germany (marked with Ω on the map in Fig. 2.7) in dependence of the forecast time. Differences between simulation and observation during the afternoon while they match in the morning are obvious.

Time series for the aerosol optical thickness τ , the radiative flux of shortwave (F_{sw}) and longwave (F_{lw}) radiation, the average in-cloud vertical velocity (w_{cloud}), the liquid (LWP)

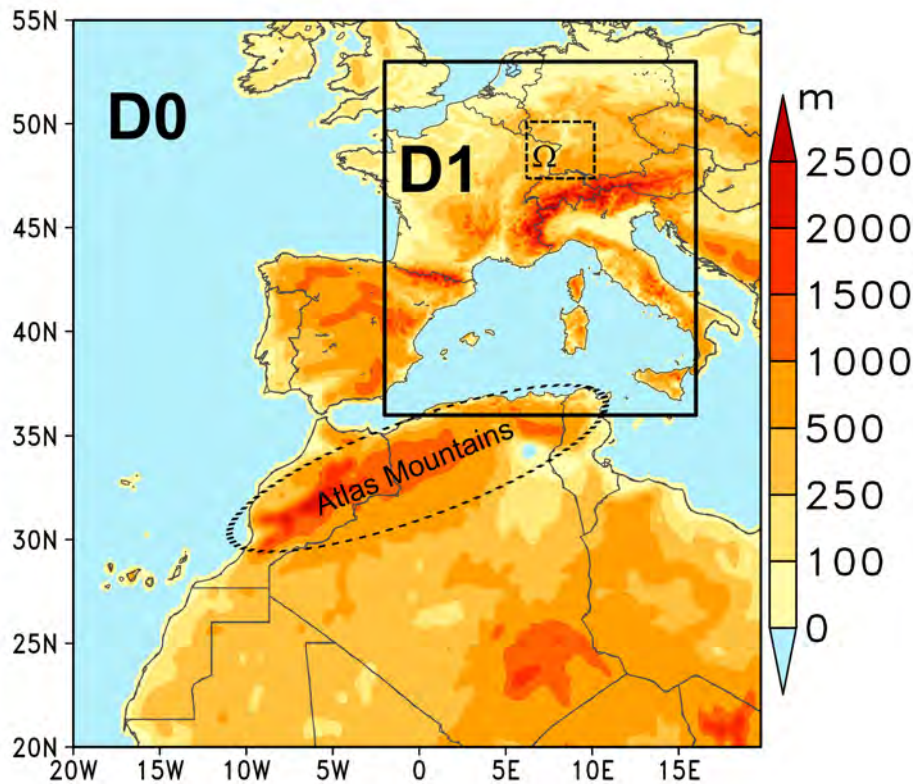


Figure 2.7: Topological map with the domains D0, D1, and Ω [Bangert et al., 2012].

and ice water path (IWP) as well as T_{2m} have been calculated. Figure 2.9 shows the averaged results for the domain D1 for the different simulations for the whole time period. For the maximum of the aerosol optical thickness (Fig. 2.9 top left) on the 27th of May 2008 ($\tau_{max} \approx 0.3$) the Lambert-Beer law [Atkins and de Paula, 2002] yields a percentage of radiation which was affected by dust of about 30%. In the remaining graphs in Figure 2.9 the solid black line represents simulation C, the dashed black line simulation REF, the solid gray line simulation CR, and the dotted gray line simulation R. The orange shadings identify positive deviations between C and REF, blue shadings negative ones. The direct effect caused by mineral dust can be seen in the plot of the longwave and shortwave radiation (Fig. 2.9 top right): Simulations that include the direct effect (CR + R) compared to the simulations that exclude this effect (REF + C) are shifted during the whole time period by a more or less constant negative value. The systematical deviation of T_{2m} (Fig. 2.9 bottom right) can be explained by the indirect effect.

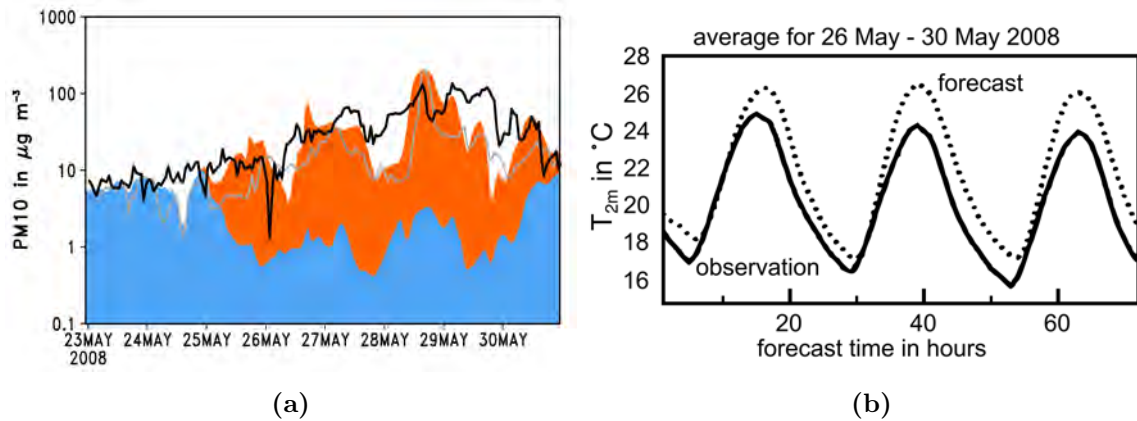


Figure 2.8: 2.8a represents the measured and simulated aerosol mass concentration, PM_{10} , between the 23rd and the 30th of May 2008. Black solid line for measurements at Hohenpeissenberg, Germany, grey solid line for simulation of domain D1 and shadings for simulation of domain D0. In Figure 2.8b the anomalies between simulated and measured temperature in area Ω for the period from 26th till 30th May are shown [Bangert et al., 2012].

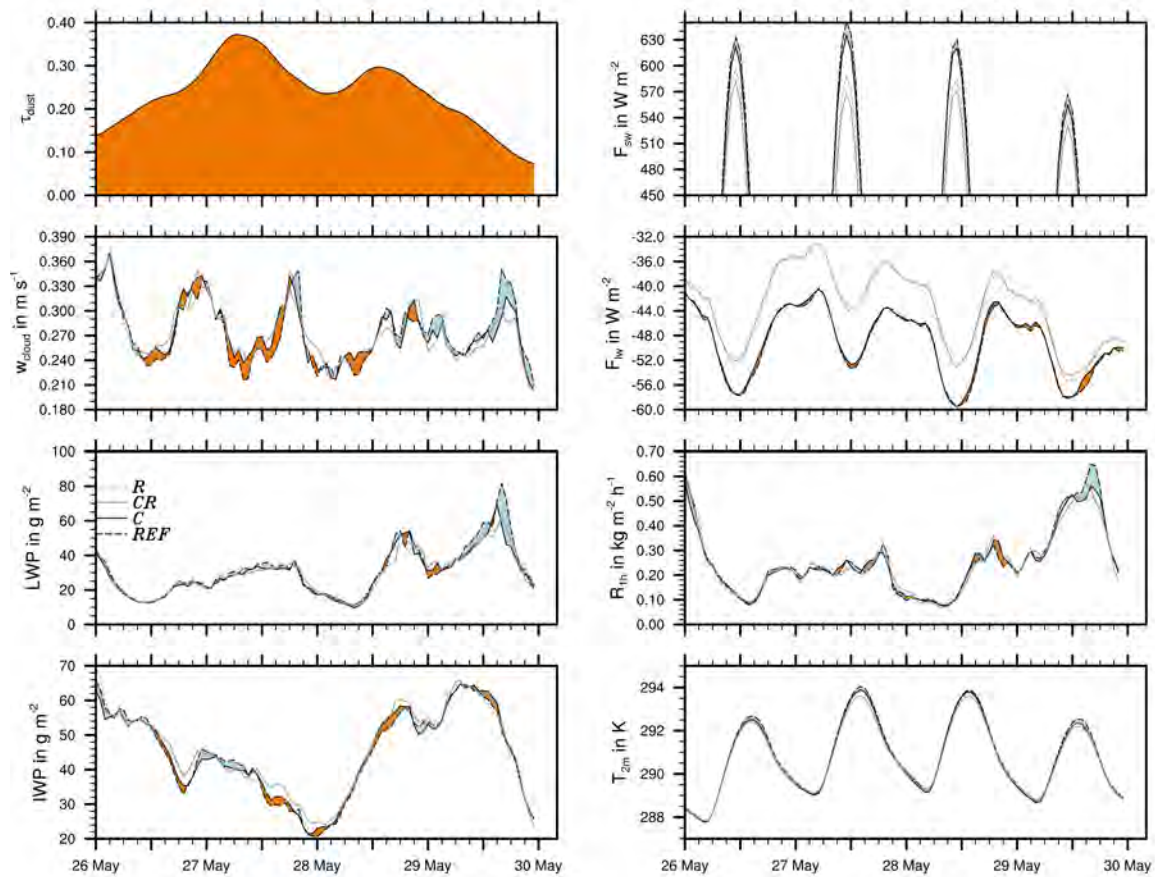


Figure 2.9: Results for the domain D1 shown in Figure 2.7 adopted from *Bangert et al.* [2012]. Left column from top down: Aerosol optical thickness (τ), vertical velocity inside the clouds (w_{cloud}), liquid water path (LWP) and ice water path (IWP); right column from top down: radiant flux of shortwave radiation at surface (F_{sw}), radiative flux of longwave radiation at surface (F_{lw}), hourly precipitation rate (R_{1h}), and the 2-m temperature (T_{2m}). Solid lines represent simulations C (black) and CR (grey) while the dashed lines represent simulations REF (black) and R (grey).

Chapter 3

Ground-Based Observation of Cloud Parameters

In terms of model-to-observation evaluations precise measurements are necessary. These measurements either can be sampled in-situ by airborne or ground-based methods or by remote-sensing instruments. Airborne measurements have the disadvantage to be fixed to a certain height and limited in time while remote sensing approaches are able to provide continuous measurements in numerous height levels. In this study data provided by the multi-instrument platform LACROS [Wandinger, 2012] at TROPOS in Leipzig is used. LACROS comprises several active and passive remote-sensing instruments which are shown in Figure 3.1. Mentionable for this study are especially Light Detection and Ranging (lidar,

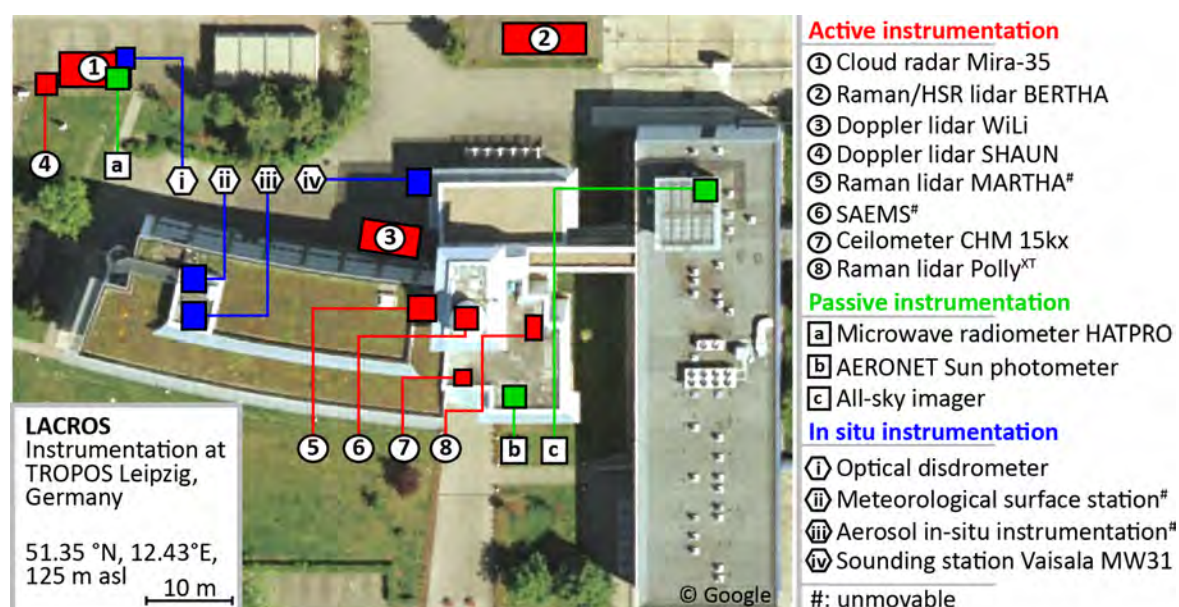


Figure 3.1: Instrumentation of LACROS at TROPOS [TROPOS, 2016]. Used in this study is data from the cloud radar Mira-35 (1), the lidar ceilometer CHM 15kx (7) or the raman lidar Polly^{XT} (8), and the microwave radiometer HATPRO [a].

ceilometer CHM 15kx (7) or Polly^{XT} (8)), Cloud Radio Detection and Ranging (cloud-radar, Mira-35 (1)), and microwave radiometer (HATPRO [a]) since to observe the full troposphere column in a reasonable resolution, instrument synergies must be used. Lidar measurements are suitable to determine small particles while a cloud radar is sensitive to bigger ones, and a microwave radiometer is able to determine the liquid water path. The mode of their operation will be explained within this Chapter.

To analyze the data and to determine the appropriate cloud parameters an algorithm introduced by *Illingworth et al.* [2007] is applied at TROPOS. This algorithm is used at several stations in Europe which are organized in the Cloudnet network [*Illingworth et al.*, 2007], to determine homogeneous cloud properties by lidar, cloud-radar and microwave radiometer measurements. Due to its more descriptive explanation an algorithm by *Shupe* [2007] to classify cloud phase on the base of ground-based observations, which is comparable to the Cloudnet approach, will be presented. It uses the lidar to identify ice and liquid water clouds, the cloud-radar to derive large particles, and the multichannel microwave radiometer to estimate the column-integrated liquid water path (LWP). Since 2011 the LACROS instrument site at the Leibniz Institute for Tropospheric Research (TROPOS) in Leipzig is part of the Cloudnet network and collects continuous recordings about the vertical structure of cloud and aerosol layers [*TROPOS*, 2016].

3.1 Light Detection and Ranging (Lidar)

The mode of operation of a lidar is dedicated to the detection of the amount of radiation of an emitted laser pulse that is scattered back to the emitter. Depending on the application different wavelengths between 250 nm and 11 μm are used [*Weikamp*, 2005]. The laser light is scattered and reflected by particles in the atmosphere. Based on the generalized active remote sensing equation:

$$P_c(R) = \frac{C}{R^2} O(R) \beta(R) T(R) \quad (3.1)$$

the backscatter coefficient $\beta(R)$ and the transmission term $T(R)$ of a scattering volume at a distance R can be determined. $P_c(R)$ is the detected signal at the instrument. C is a system constant including, amongst other system parameters, the emitted power P_0 and $O(R)$ represents the overlap function, which can be traced back to the instrument geometry since transmitter and receiver are usually not on the same spot.

The transmission can be described by the Lambert-Beer law [*Atkins and de Paula*, 2002] as:

$$T(R) = \exp\left(-2 \int_0^R \alpha(R') dR'\right). \quad (3.2)$$

and is connected to the backscatter coefficient via the extinction coefficient α by the

extinction-to-backscatter ratio:

$$L = \frac{\alpha}{\beta}. \quad (3.3)$$

Both backscatter coefficient and extinction coefficient can for example be derived by methods introduced by *Ansmann et al.* [1990].

To derive further information about the shape of the particles the depolarization ratio δ is used. To determine δ the received signal is measured in two channels simultaneously with perpendicular polarization sensitivity, while the emitted signal is completely polarized in one of these planes. The linear depolarization ratio is given by the quotient of the measured signal of the perpendicular channel to the parallel channel:

$$\delta = \frac{P_{\perp}}{P_{\parallel}}. \quad (3.4)$$

The depolarization ratio allows to draw conclusions about the shape of the particles. Signal reflected by spherical particles is rather less depolarized than signals reflected by non-spherical ones, since a spherical shape mostly creates single-scattering while a non-spherical shape generate multiple scattering [*Sassen*, 1984].

The continuous determination of the backscatter coefficient and extinction coefficient is usually complicated because the atmospheric transmission $T(R)$ varies strongly as a function of aerosol type and concentration. Therefore typically the so-called attenuated backscatter coefficient β_{att} is used as lidar observable:

$$\beta_{\text{att}} = \frac{P_c(R)R^2}{CO(R)} = \beta(R) \cdot T(R). \quad (3.5)$$

β_{att} is the product of the two atmospheric parameters extinction and backscatter coefficient, calibrated with respect to all range-dependent and instrumental effects. For a clean atmosphere with a high transmission ($T(R)$ approaches 1) the attenuated backscatter coefficient is equal to the backscatter coefficient.

The backscatter coefficient β as well as the attenuated backscatter coefficient β_{att} depends strongly on the effective surface of the scattering particle. The signal of several small particles which have combined a large surface can superimpose the radiation backscattered by fewer large particles. Since even small particles scatter a great amount of the emitted radiation the intensity decreases strongly after a small distance within a cloud and there are partial barely any lidar signals from inside a cloud. Consequently lidar measurements are useful to determine the cloud base, especially the base of liquid cloud layers, and ice crystals inside the cloud but it is usually not possible to image the whole atmosphere [*Shupe*, 2007]. The ceilometer CHM 15kx operates with a wavelength of 1064 nm and the Polly^{XT} at wavelengths of 355 nm, 532 nm, and 1064 nm.

3.2 Cloud Radio Detection and Ranging (Cloud Radar)

The principle of a cloud radar is similar to a lidar using a larger wavelength. Typically about 5000 radio wave pulses per second with a frequency of 35 or 94 GHz are emitted into the atmosphere. Within this study a cloud radar with a frequency of 35 GHz is used. The attenuation of radar radiation is due to its larger wavelength smaller than for a lidar. The received signal $P(R)$ can be described by the radar equation:

$$P(R) = \frac{P_t \pi^2 \lambda^2 \Delta R}{16 \varphi^2} R^{-2} T(\vec{R}) \eta. \quad (3.6)$$

R is the distance to the scattering particle and η its specific backscattering cross section or reflectivity. T represents the transmission in between. P_t is the emitted power and can be combined with the wavelength λ and the beamwidth φ to a system constant [*Peters and Görndorf, 2011*]:

$$C = \frac{P_t \pi^2 \lambda^2 \Delta R}{16 \varphi^2}. \quad (3.7)$$

By means of the Rayleigh approximation the reflectivity can be expressed by:

$$\eta = \frac{\pi^5}{\lambda^4} K^2 Z \quad (3.8)$$

with $K = |(m^2 - 1)/(m^2 + 2)|$, where m is the complex refractive index. Z is the reflectivity factor, which is called effective radar reflectivity factor Z_e if not only liquid water droplets are present in the scattering volume and can be determined by the cloud radar measurements. Besides Z_e , the mean Doppler velocity V_D and the width of the Doppler spectrum W_D are calculated and used to detect stacked cloud layers [*Peters and Görndorf, 2011*].

The effective reflectivity factor Z_e is proportional to the sixth power of the particle size D :

$$Z_e = \int_0^{D_{max}} N(D) \cdot D^6 dD, \quad (3.9)$$

where $N(D)$ is the particle size distribution density [*Peters and Görndorf, 2011*]. Hence the cloud radar is sensitive to the presence of larger particles and these signals can superimpose the signals of a high number of small particles. Thus cloud fringes and thin clouds can be missed, and the separation between ice and mixed-phase clouds is difficult [*Shupe, 2007*]. Table 3.1 lists for different particle sizes and occurrences (liquid water: [*Miles et al., 2000*], ice: [*Orikasa et al., 2013*], rain: [*Marshall and Palmer, 1948*], snow: [*Gunn and Marshall, 1958*]) the reflectivity calculated from Equation 3.9.

The Doppler velocity V_D is determined by:

$$V_D = \frac{1}{2} f_D \cdot \lambda. \quad (3.10)$$

f_D is the frequency shift induced by the Doppler effect and λ the wavelength of the emitted radiation. To determine the Doppler spectrum the velocities are assumed to be constant during a sufficient short time interval and stacked side by side [*Peters and Görndorf, 2011*].

Table 3.1: Approximated numbers of particles and diameter for liquid water, ice, rain and snow and the according values of Z_e calculated with equation 3.9.

	N in m^{-3}	D in mm	Z_e in dB
Liquid water	10^8	10^{-3} - 10^{-2}	-100 - -40
Ice	10^5	10^{-1}	-30
Rain	100	1	20
Snow	10	1 - 2	10 - 28

3.3 Microwave Radiometer

To determine the liquid water path and a vertical temperature profile, the microwave radiometer measures the thermal emission of the atmosphere in defined frequency bands. For ground-based remote sensing approaches frequencies close to the hydrogen absorption line at 22.235 GHz are usually used to identify the liquid water path whereas frequencies between 50 and 60 GHz are used for the determination of the temperature profile. Since the utilized wavelengths of the background radiation are large compared to the size of cloud droplets even signals from inside a cloud can be measured [Crewell *et al.*, 2011]. The LACROS microwave radiometer HATPRO receives 7 channels between 22 – 31 GHz and 7 channels between 51 – 58 GHz.

3.4 Cloud Classification

The Cloudnet algorithm for cloud classification is similar to an algorithm presented by Shupe [2007] which is organized in multiple steps. First aerosol, ice and liquid water is identified on the basis of lidar measurements. The next step is to use the cloud radar data to determine mixed-phase, drizzle, and snow classes as well as reclassify possible incorrect interpretations. The temperature profile and the liquid water path serve as a reference to differentiate between frozen and liquid phases. A coherence filter provides a homogenization after the classification. The Cloudnet products are provided with the vertical resolution of the radar of 30 m and a temporal resolution of 30 s. The value for one pixel results from the average of the total observations within the 30 s.

Lidar depolarization ratio δ and the backscatter coefficient β is used to separate liquid and ice water, and aerosols. The effective surface of liquid water droplets is assumed to be large compared to ice crystals since their shape usually is spherical and they appear in high number. Hence they have a high backscatter and low depolarization. A strong depolarized signal indicates the occurrence of non spherical ice crystals while in this case the backscatter coefficient normally is less intense due to the smaller number concentration. Generally the size of aerosols is assumed to be small compared to ice or liquid water droplets so that they have a low backscatter signal. Since aerosol particles occur in both spherical and non-spherical shapes they have a wide spectrum of depo-

larization. The thresholds to separate between clear sky, aerosol, ice, and liquid water introduced by *Shupe* [2007] are presented in Figure 3.2. A very low backscatter coefficient is interpreted as clean air. A low depolarization ratio or a low backscatter coefficient is characteristic for aerosol, while a high δ and a high β is considered to be ice. Only a very high backscatter coefficient with a very low depolarization ratio is interpreted as liquid water.

If the lidar classification has identified aerosol in one pixel but the cloud radar has a measurable reflectivity in the same point the pixel is reclassified as a cloud, since aerosol particles are assumed to be too small to be detected by a cloud radar. In the same manner, pixels that have been classified as liquid water but show a higher reflectivity or a higher Doppler velocity than expected for liquid droplets only ($Z_e > -17$ dBZ [*Frisch et al.*, 1995] or $V_D > 1$ m s⁻¹) are reclassified as mixed-phase or liquid+drizzle clouds for $T < 0^\circ\text{C}$ or $T > 0^\circ\text{C}$, respectively [*Shupe*, 2007]. The usage of the cloud radar reflectivity Z_e and the Doppler velocity V_D to derive certain particle types within these temperature ranges and Doppler spectrum widths is illustrated in Figure 3.3.

Cloud radar data is also used to identify unambiguous, strong precipitation periods. Pixels with $Z_e > 5$ dBZ are classified as rain ($T > 0^\circ\text{C}$) or snow ($T < 0^\circ\text{C}$). Also pixels with a temperature above the freezing point and $V_D > 2.5$ m s⁻¹ are classified as rain. Temperature thresholds are also required for the ongoing analysis of cloud radar data. If $T_{max} > 0^\circ\text{C}$ there is supposed to be no ice, while $T > T_{min} = -40^\circ\text{C}$ is determined for the occurrence of liquid water. Also the Doppler spectrum is used to identify liquid water. Statistical analysis have shown that in a wide Doppler spectrum the existence of liquid or mixed-phase are likely. Hence if $W_D > 0.4$ m s⁻¹ mixed-phase or rain is identified. Only if a high reflectivity is measured ($Z_e > 5$ dBZ) liquid water is supposed to be not possible [*Shupe*, 2007].

Liquid water that neither has been detected by lidar nor by cloud radar can be identified from the liquid water path (LWP) measured with the microwave radiometer. If $LWP \geq 25$ g m⁻² and no liquid water was classified so far a liquid water layer has to be defined.

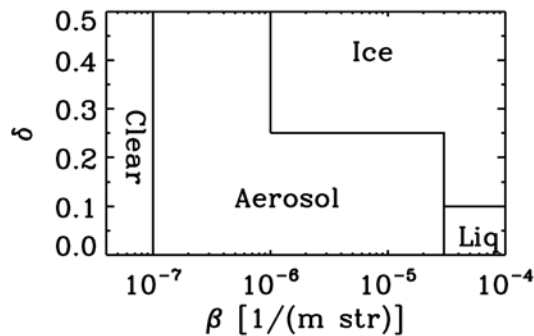


Figure 3.2: Initially classification scheme for lidar backscatter and depolarization [*Shupe*, 2007].

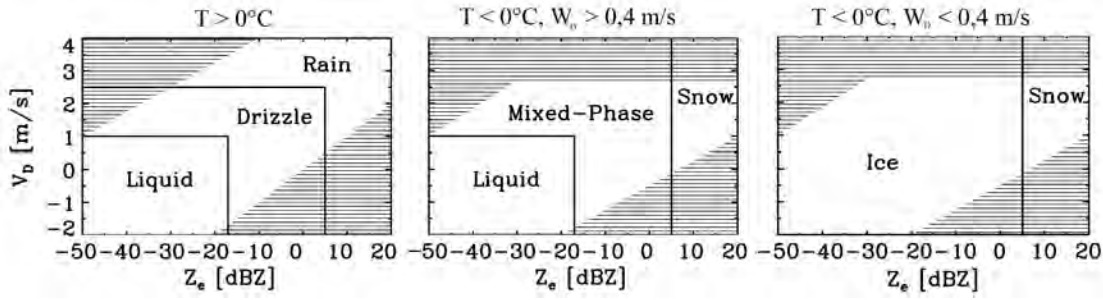


Figure 3.3: Classification scheme for cloud radar reflectivity, Doppler velocity and spectrum. Left for $T > 0^\circ\text{C}$, center for $T < 0^\circ\text{C}$ and $W_D > 0.4\text{ m s}^{-1}$, and right for $T < 0^\circ\text{C}$ and $W_D < 0.4\text{ m s}^{-1}$ [Shupe, 2007].

This threshold is derived from the uncertainty of the microwave radiometer. If on the other hand $LWP \leq 0\text{ g m}^{-2}$ and $T < 0^\circ\text{C}$ all liquid-containing pixels in this column are set to ice [Shupe, 2007].

Figure 3.4 shows an example for a measurement at the Cloudnet site Leipzig from the 5th of April 2014. Top down represented are cloud radar reflectivity, Doppler velocity, Doppler spectrum width, lidar depolarization, lidar attenuated backscatter coefficient, precipitation rate and liquid water path. The different sensitivities of the measuring instruments for different particle types are identifiable (lidar: lower cloud layers; cloud radar: clouds with large liquid or ice particles). The classification derived by these measurements is presented in Figure 3.5a, while Figure 3.5b shows on the basis of which data the classification has been done. For instance the aerosol layer (grey regions in Figure 3.5a) has almost exclusively been identified by lidar measurements while ice clouds (yellow and green regions) and liquid water droplets (blue and light blue regions) mostly can be traced back to cloud radar data. Precipitation (red regions) was detected by lidar as well as by cloud radar.

3.5 Retrieval of Cloud Microphysical Properties

The observed parameters in combination with the retrieved target categorization mask are utilized to determine the liquid water content, ice water content, and the cloud fraction. In doing so algorithms from the Cloudnet package are applied to the data, as described in Illingworth *et al.* [2007]. In here, only a brief overview on the retrieval of ice water content and liquid water content will be provided.

The determination of IWC is based on Hogan *et al.* [2006]. They derived a parameterization for the IWC as a function of radar reflectivity (see Eq. 3.9) and temperature. For a cloud radar using a wavelength of 35 GHz this yields:

$$\log_{10}(IWC) = 2.42 \cdot 10^{-4} ZT + 6.99 \cdot 10^{-2} Z - 1.86 \cdot 10^{-2} T - 1.63. \quad (3.11)$$

The parameterization is predicated on a comparison between aircraft in-situ observations of ice crystals and co-located radar observations. To calculate the IWC, the temperature is taken from the model data which is available for Cloudnet and the reflectivity is provided by the cloud radar observations as described in Section 3.2. In Figure 3.6a the retrieved IWC by Cloudnet algorithms for the 5th of April 2014 for Leipzig is presented.

The determination of the cloud liquid water content is based on the assumption that changes inside clouds occur only adiabatic. Between any pair of liquid cloud base and cloud top derived from the Cloudnet target categorization, the LWC is calculated based on the assumption that adiabatic conditions were present within the liquid layer. Thus, the LWC increases linearly with height, starting at zero at cloud base [Albrecht *et al.*, 1990]. Cloudnet in addition provides the so-called scaled adiabatic liquid water content that is derived when co-located observations of the liquid water path (LWP) are available. In this case, the adiabatic liquid water content is normalized in such a way that the total LWP of the liquid layers in a Cloudnet profile equals the LWP observed with the microwave radiometer. This technique allows to infer the cloud adiabaticity, which is an important parameter for satellite-based studies of liquid water clouds [Merk *et al.*, 2016]. For the model evaluation however the unscaled adiabatic profiles are used. Figure 3.6b shows the scaled LWC determined by Cloudnet for the 5th of April 2014 for Leipzig.

The cloud fraction is derived as the ratio of the of the 30 m height and 30 s lasting pixels in the observed column categorized either as liquid, supercooled, or ice cloud. When scaling the observations on the model grid, which is described in more detail in 5.1.3, all pixels within one model layer yield the cloud fraction.

In Chapter 6 and 7 the cloud fraction, the liquid water content, and the ice water content will be used to determine the impact of mineral dust on the predictability of clouds and cloud properties by NWP models.

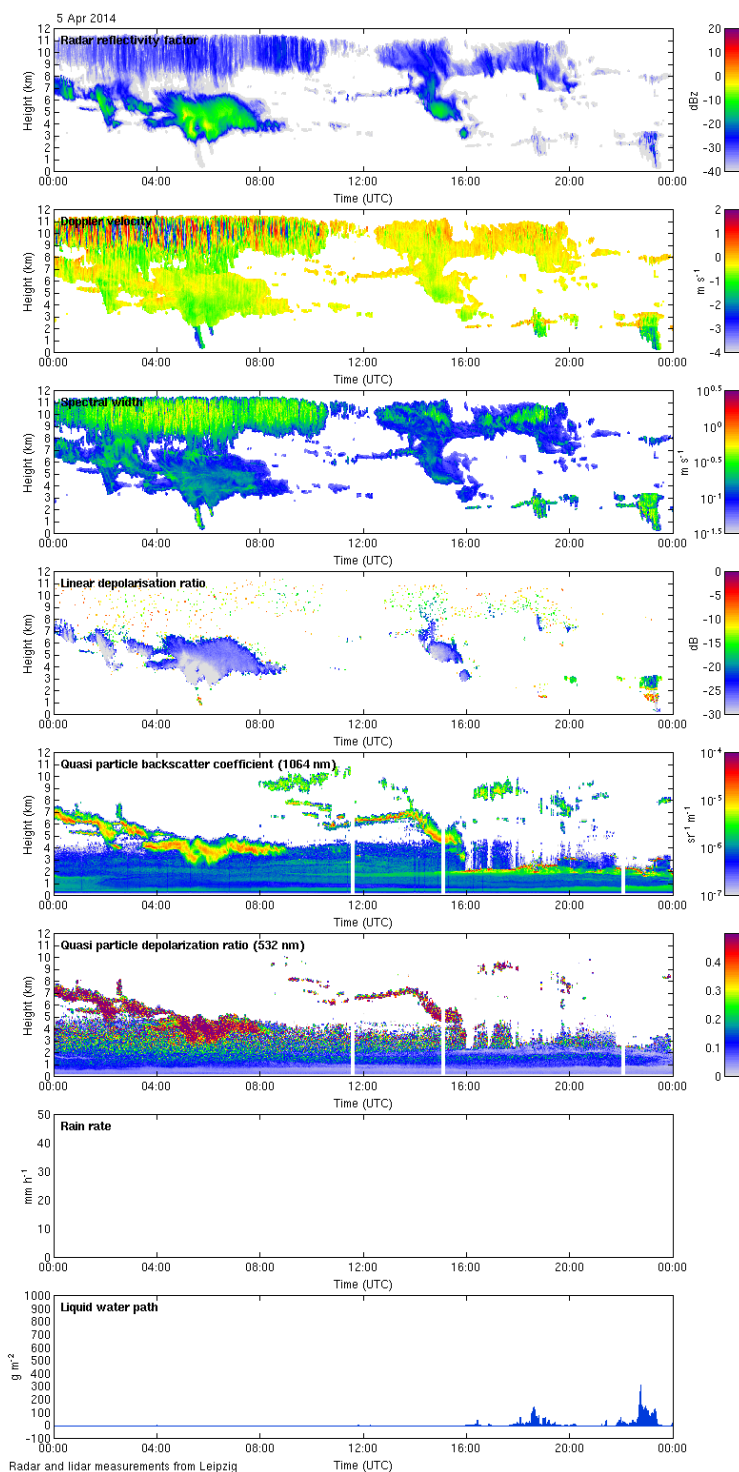


Figure 3.4: Cloudnet measurements for the 05th of April 2014 at Leipzig [Cloudnet, 2016]. From top down: radar reflectivity factor, Doppler velocity, spectral width, and linear depolarization ratio measured with the cloud radar and particle backscatter coefficient at 1064 nm, and particle depolarization ratio at 532 nm measured with lidar as well as rain rate observed with a rain gauge, and liquid water path derived from the microwave radiometer measurements.

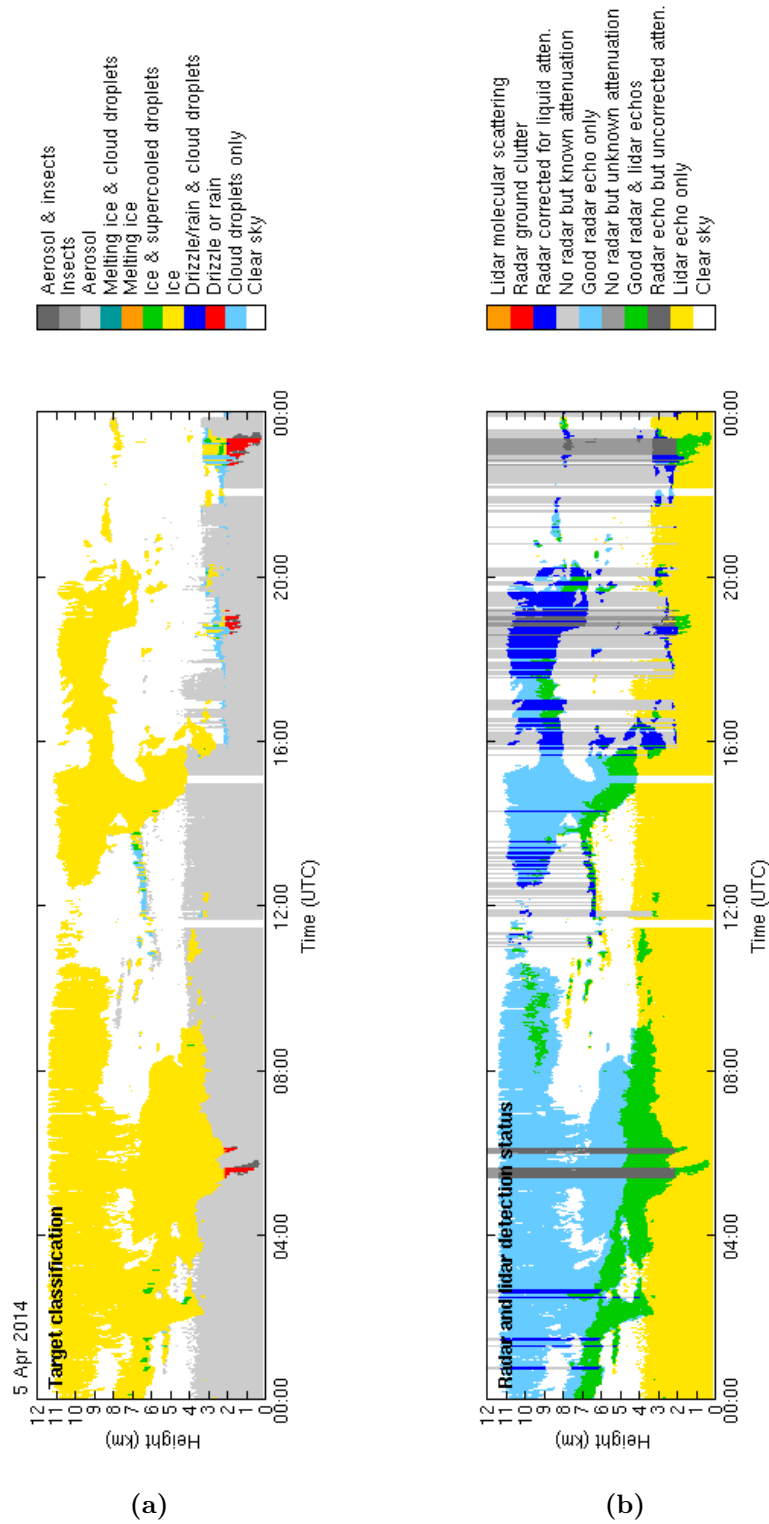


Figure 3.5: Cloudnet classification scheme for the measurements on the 05th of April 2014 at Leipzig shown in Figure 3.4 [Cloudnet, 2016]. (a) shows the resulting classification and (b) on which measurements the classification is based on.

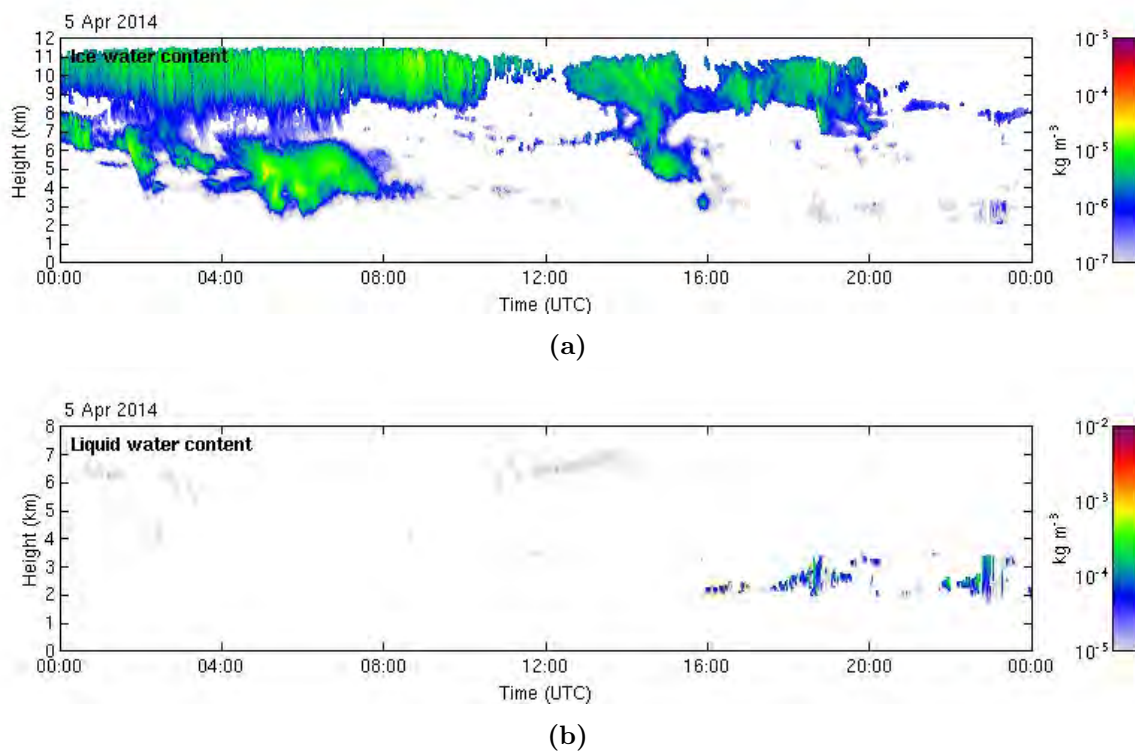


Figure 3.6: IWC and LWC determined by Cloudnet for the 5th of April 2014 for Leipzig. (a) represents the IWC and (b) shows the correspondent scaled LWC.

Chapter 4

Model Data

Since *Abbe* [1901] and *Bjerknes* [1904] first proposed the idea to use the law of physics in terms of weather prediction numerous numerical weather prediction models have been developed. These models are characterized by their spatial and temporal resolution, and the representation of the laws of physics. The physical processes can either be represented by equations which have to be solved to calculate the future state of the atmosphere on each model grid point or on the other hand by parametrizations. Typically processes that are too small-scale or too complex to be solved explicitly are parametrized. For this study the NWP models COSMO-EU, COSMO-DE and ECMWF-IFS will be analyzed and their basic principles will be introduced within this Chapter.

4.1 Consortium for Small-scale Modeling (COSMO)

The operational NWP model of the German weather service (DWD) for Europe and Germany Consortium for Small-scale Modeling (COSMO) is a nonhydrostatic fully compressible atmospheric prediction model which has been developed for both operational numerical weather prediction and various scientific applications on a wide range of spatial resolutions. It is based on the primitive thermo-hydrodynamical equations describing compressible flow in a moist atmosphere [*Doms and Baldauf*, 2015]. Physical processes are included using parametrizations. Clouds, aerosol, and more gaseous trace matter are considered as optical active components of the atmosphere which influence the radiative transfer by absorption, emission and scattering. Such as taking effects caused by aerosols into account the COSMO-Model assumes a constant aerosol climatology as described by *Tegen et al.* [1997]. Twelve monthly mean values for aerosol in rural, urban or desert areas and over sea are assumed [*Schättler and Blahak*, 2015].

4.1.1 COSMO-EU

The local model COSMO-EU covers whole Europe with a rotated latitude/longitude grid ranging from $\lambda_g = 09.14^\circ \text{W}$, $\varphi_g = 27.70^\circ \text{N}$ to $\lambda_g = 63.47^\circ \text{E}$, $\varphi_g = 62.40^\circ \text{N}$

with its North Pole at $\lambda_N = 170.0^\circ$ W and $\varphi_N = 40.0^\circ$ N. The horizontal grid is composed of $665 \times 657 = 436905$ grid points with a resulting horizontal resolution of $\Delta\lambda = \Delta\varphi = 0.00625^\circ \approx 7$ km. The vertical structure of the atmosphere is modeled up to a height of ~ 24 km in 40 primary and 41 secondary time-invariant layers. Close to the ground the layers are parallel to the surface while they are horizontally stratified in the stratosphere. The lowermost 12 km of the atmosphere over Leipzig which are relevant for this study are modeled in 33 primary layers. COSMO-EU forecasts for cloud fraction, ice water content, and liquid water content are available at an hourly interval with forecast times (time since start of the model forecast) between 0 and 71 hours [Schulz and Schättler, 2014]. During this study the model results from COSMO-EU with forecast times of 3 – 5 hours have been used.

4.1.2 COSMO-DE

COSMO-DE is a local model used by the DWD and covers whole Germany, Switzerland, and Austria and partially the neighboring states. It consists of $421 \times 461 = 194081$ horizontal grid points on 50 layers reaching a height of 22000 m above sea level, whereas 38 layers are located in the lowermost 12 km of the atmosphere. Same as for COSMO-EU the North Pole is defined at $\lambda_N = 170.0^\circ$ W and $\varphi_N = 40.0^\circ$ N. The horizontal grid extends from $\lambda_g = 02.98^\circ$ E, $\varphi_g = 44.77^\circ$ N in the south west and $\lambda_g = 17.72^\circ$ E, $\varphi_g = 44.72^\circ$ N in the south east to $\lambda_g = 01.04^\circ$ E, $\varphi_g = 56.20^\circ$ N in the north west and $\lambda_g = 19.84^\circ$ E, $\varphi_g = 56.14^\circ$ N in the north east. The resulting horizontal resolution yield 2.8 km. Thus COSMO-DE exhibit a higher horizontal and vertical resolution compared to COSMO-EU. COSMO-DE provides predictions of cloud fraction, ice water content, and liquid water content with forecast times between 0 and 27 hours with an hourly interval [Baldauf *et al.*, 2014]. The model results of COSMO-DE used in this study have forecast times of 3 – 5 hours.

4.2 European Centre for Medium-Range Weather Forecasts — Integrated Forecast System (ECMWF-IFS)

The Integrated Forecast System (IFS) is a global NWP model [ECMWF, 2016]. It has been developed and operated by the European Centre for Medium-Range Weather Forecasts (ECMWF), an intergovernmental organization supported by most of the nations of Europe. Its horizontal grid has a resolution of 16 km and the vertical grid is divided into 137 levels that reach up to 22700 m above sea level. About 64 layers are located in the lowermost 12 km. At ground level these layers follow the topography but with increasing height they get horizontal with height $z = \text{const}$. Similar to the COSMO models ECMWF-IFS uses the aerosol parametrization from Tegen *et al.* [1997] and does not respect daily variations in the aerosol concentration. For this study model results with forecast time of 12 – 37 hours have been used.

Chapter 5

Methodology

The aim of this study is to identify the effect mineral dust can have on the predictability of cloud properties by NWP models. In the following section the approach used to evaluate the model results is presented.

5.1 How to Determine the Effect of Mineral Dust Aerosol on the Predictability of Clouds and Cloud Properties by Numerical Weather Prediction Models?

To determine the effect of mineral dust on the predictability of cloud fraction and IWC by NWP models, model results from COSMO-EU, COSMO-DE, and ECMWF-IFS for a major dust event in spring 2014 at Leipzig will be compared to observations from LACROS at TROPOS. This event is separated according to the atmospheric dust concentration into dust-laden and low-dust days. The dust concentration is determined by the atmospheric dust forecast system BSC-DREAM8b v2.

In addition, in a long-term study the COSMO-EU and COSMO-DE cloud fraction, IWC, and LWC forecasts for Leipzig during a period from September 2011 until June 2014 will be analyzed. This time period is split according to the dust concentration simulated by BSC-DREAM8b v2 in defined temperature regimes. The model results will be compared to LACROS observations at TROPOS within each period and an intercomparison between the different situations will be done.

5.1.1 Identification of Dust-Laden Episodes: BSC-DREAM8b v2

The Dust Regional Atmospheric Model BSC-DREAM8b v2 [Pérez *et al.*, 2006a,b; Basart *et al.*, 2012] (DREAM) is an integrated modeling system to predict the atmospheric life cycle of eroded desert dust developed by the Barcelona Supercomputing Center - Centro Nacional de Supercomputacin. It provides among other parameters the dust concentration

in a vertical resolution of 24 eta-levels up to a height of 15 km and a horizontal resolution of $1/3^\circ$. Its spatial coverage ranges from 25° W, 0° N to 60° E, 65° N. DREAM has already been used by *Seifert et al.* [2010] to evaluate the effect of dust on heterogeneous ice formation at Leipzig.

5.1.2 Dust Concentration - Temperature Grid

The goal of the long-term study is to check if the performance of the forecast models varies between dust-laden and dust-free conditions, and how these differences are visible in several temperature regimes. Thus, 4 different temperature regimes were defined that determine specific conditions for cloud formation. These regimes were characterized by $T > 0^\circ\text{C}$, $0^\circ\text{C} > T > -25^\circ\text{C}$, $-25^\circ\text{C} > T > -40^\circ\text{C}$, and $T < -40^\circ\text{C}$. The cloud-microphysical reasoning for selecting these temperature regimes is as follows. At $T > 0^\circ\text{C}$ only liquid-water clouds can form and ice formation should not be affected. Between 0°C and -25°C , ice formation is limited to liquid-phase processes, i.e., ice forms predominantly from supercooled liquid droplets as it was found by *Ansmann et al.* [2009], *de Boer et al.* [2011] and *Westbrook and Illingworth* [2011]. No deposition freezing takes place. This is different for $-25^\circ\text{C} > T > -40^\circ\text{C}$, where liquid-dependent ice nucleation and deposition nucleation can take place. At a temperature below -40°C , liquid-droplet formation is absent and ice formation is limited to either deposition nucleation or homogeneous nucleation.

For the defined temperature regimes, dust-laden, low-dust and dust-free days were derived from profiles of dust-concentration simulated with DREAM. To do so, the height-grid of DREAM was converted into a temperature profile based on the nearest height-temperature profile available from COSMO-EU. Dust-laden cases were defined by a threshold of $c_{D_{crit}} = 2 \mu\text{g m}^{-3}$. In order to be classified as dust-free, the dust concentration at all heights within a temperature interval had to be $c_D = 0 \mu\text{g m}^{-3}$. Days with intermediate conditions have been considered as low-dust.

Two properties of the dust classification scheme should be noted. First, the separation is done on a daily basis, because Cloudnet provides daily outputs. Second, on a specific day, the defined thresholds may be met in several temperature regimes. Restricting the data analysis to days where the thresholds were only met in a single temperature regime would have reduced the dataset statistics too much.

The resulting data set for the cloud fraction is illustrated in Table 5.1. In Figure 7.1 the maximum dust concentration for Leipzig on each day during the whole time period from September 2011 until June 2014 for every temperature regime is presented and further discussed in Chapter 7.

To analyze a dust outbreak over Leipzig in spring 2014 model and observational data from the 29th of March until the 28th of April 2014 have been used. This data set was

Table 5.1: Number of days during the long-term analysis that showed the corresponding dust concentration in the respective temperature range when cloud fraction data was available for COSMO-EU.

	Dust-free $c_D = 0 \mu\text{g m}^{-3}$	Low-dust $0 > c_D > 2 \mu\text{g m}^{-3}$	Dust-laden $c_D > 2 \mu\text{g m}^{-3}$
$T > 0^\circ\text{C}$	59.9	433.2	137.8
$0^\circ\text{C} > T > -25^\circ\text{C}$	61.2	466.8	139.4
$-25^\circ\text{C} > T > -40^\circ\text{C}$	103.3	514.9	50.2
$T < -40^\circ\text{C}$	116.8	522.3	29.3

manually separated due to the dust concentration in any altitude up to 12 km.

5.1.3 Scaling of Measurements on Model Grid

Thanks to the combination of lidar, cloud-radar and microwave radiometer Cloudnet provides a spatial resolution with height of 30 m and a temporal resolution of 30 s. Since neither the spatial nor the temporal resolution of any model is comparable to this, the Cloudnet data will be scaled down on the relevant model grid. The scaling procedure within Cloudnet, that is outlined in *Illingworth et al.* [2007] is based on previous developments documented by *Mace et al.* [1998] and *Hogan et al.* [2001]. In doing so the measurements will be averaged over time and height and weighted with the wind velocity to get a mean value for the whole model grid box and for each model layer. All statistical analyses have been made with scaled observations on the corresponding grid, but nevertheless only observations scaled on the ECMWF-IFS grid will be shown in Chapter 6 (the observations scaled on the corresponding grid for COSMO-EU and COSMO-DE are attached in the Appendix A).

5.1.4 Statistical Analysis

To evaluate the effect of mineral dust on the predictability of the cloud properties, the data set of each period was individually analyzed using Cloudnet algorithms, which are introduced in Chapter 3.5. After that the statistical analysis of the modeled cloud fraction, IWC or LWC was on the one hand compared to the observations. On the other hand the results of the different models were checked against each other within the different dust concentration and temperature ranges. Cloudnet has already been applied for the evaluation of model forecasts based on long-term continuous ground-based remote sensing. For instance *Bouniol et al.* [2010] used observations of the ice water content to evaluate respective model forecasts.

Chapter 6

Dust Outbreak Spring 2014

In spring 2014 a major dust event reached Leipzig with dust concentrations $c_D > 10^{-8} \text{ gm}^{-3}$ [DREAM, 2015]. This event will be presented in this Chapter as a case study to analyze the effect of mineral dust on the predictability of cloud fraction and ice water content from COSMO-EU, COSMO-DE, and ECMWF-IFS. In doing so the period from the 29th of March until the 28th of April 2014 has been categorized into dust-laden and low-dust days. For the cloud fraction analysis 12.6 days have been considered as dust-laden and 17.5 days as low-dust for both COSMO models and 12.7 days as dust-laden as well as 17.5 as low-dust for ECMWF-IFS. To analyze the IWC from the COSMO-EU (COSMO-DE) data 11.5 (11.3) days were categorized as dust-laden and 15.6 (15.2) as low-dust. For the analysis of the EWMF-IFS forecast 11.9 dust-laden and 16.8 low-dust days have been considered. The differences in the number of days between the three models are due to missing model data.

In Figure 6.1, showing the time height cross section of the dust concentration simulated with DREAM [2015] over Leipzig, the dust-laden period between the 29th of March until the 9th of April is striking. It is characterized by four main plumes. The first is already diminishing on the 29th of March. On the 30th the next plume approaches and stays in the upper troposphere until the 1st of April. The third follows on the 3rd of April which reaches on the 4th up to 12 km height and diminishes on the 6th. The last one is not as distinct as

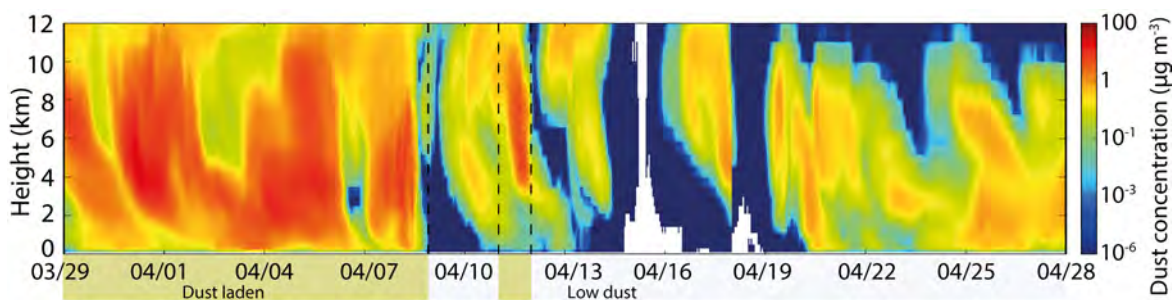


Figure 6.1: Simulated dust concentration during outbreak over Leipzig in March and April 2014 [DREAM, 2015]

the other three are and is mostly limited to the lower 7 kilometers. It approaches on the 7th and diminishes during the 8th. This period is followed by two days with lower dust concentration and on the 11th another dust plume emerges at heights between 4 and 10 km. The remaining period from the 12th until the 28th of April exhibits no considerable dust concentration. However it is hardly dust-free and thus classified as low-dust. In contrast to the long-term analysis presented in Chapter 7 for the dust concentration separation the whole column has been considered for the separation of dust-laden and low-dust days, respectively.

Figure 6.1 provides an overview on the dust conditions during the discussed time period. The observations and model results for cloud fraction and ice water content for this period are represented in Figure 6.2 and 6.3, respectively. The top row of each Figure shows the Cloudnet observations scaled on the ECMWF-IFS model grid (the observations scaled on the COSMO-EU and COSMO-DE grid are shown in the Appendix A). In the second and third row the model results from COSMO-EU and COSMO-DE are presented, respectively. The last row shows the model results from ECMWF-IFS. White spaces in the observations are due to interruptions in measurements and these periods have not been considered in the statistical analysis.

The cloud fraction forecast (Fig. 6.2) during the whole time period from COSMO-EU and COSMO-DE show only small differences. The resolution of both models decreases with altitude, with a stronger decline for COSMO-EU. Between the 30th of March until the 8th of April (all days that have been classified as dust-laden) both model forecasts show an almost constant cirrus layer around 11 km height. Differences are noticeable in the lower clouds. While COSMO-DE is able to reproduce these clouds quite reasonable COSMO-EU fails in modeling them, e.g., between the 11th and the 16th of April. If clouds are predicted, both models tend to forecast a cloud fraction of 1.0 while the observations show lower values more often. While ECMWF-IFS reproduces the low clouds mostly quite well it underestimates the cloud fraction at above 2 km height to a large extent.

In Figure 6.4 the statistical analysis for both cloud fraction and ice water content is presented. Both periods (dust-laden and low-dust) have been individually evaluated and these analyses are highlighted in the same color as the dust-laden or low-dust days in Figure 6.1, respectively. Figure 6.4a shows the cloud fraction analysis from left to right for COSMO-EU, COSMO-DE, and ECMWF-IFS, respectively. In blue the observations, in purple the model results and in red the model results without ice cloud considered to be below the radar sensitivity threshold are presented. To calculate the undetectable ice clouds the known minimum detectable radar reflectivity was converted into a minimum detectable ice-water-content-height function (for more information on the detection threshold see *Bühl et al.* [2016]). To remove the undetectable IWC the equation introduced by *Hogan and Illingworth* [2003] was used. The dashed red line includes snow and is only present in the

plots for ECMWF-IFS, since this model treats ice clouds and snow separately and does not consider snow in the cloud fraction or IWC [Hogan *et al.*, 2001]. The same coloring is used in Figure 6.4b for the ice water content analysis. Additionally the grey line represents the model results including these periods where no observational data was available.

An underestimation of high-altitude clouds from ECMWF-IFS is obvious, as shown in Figure 6.2 while the observations of the low clouds are quite reasonable depicted by

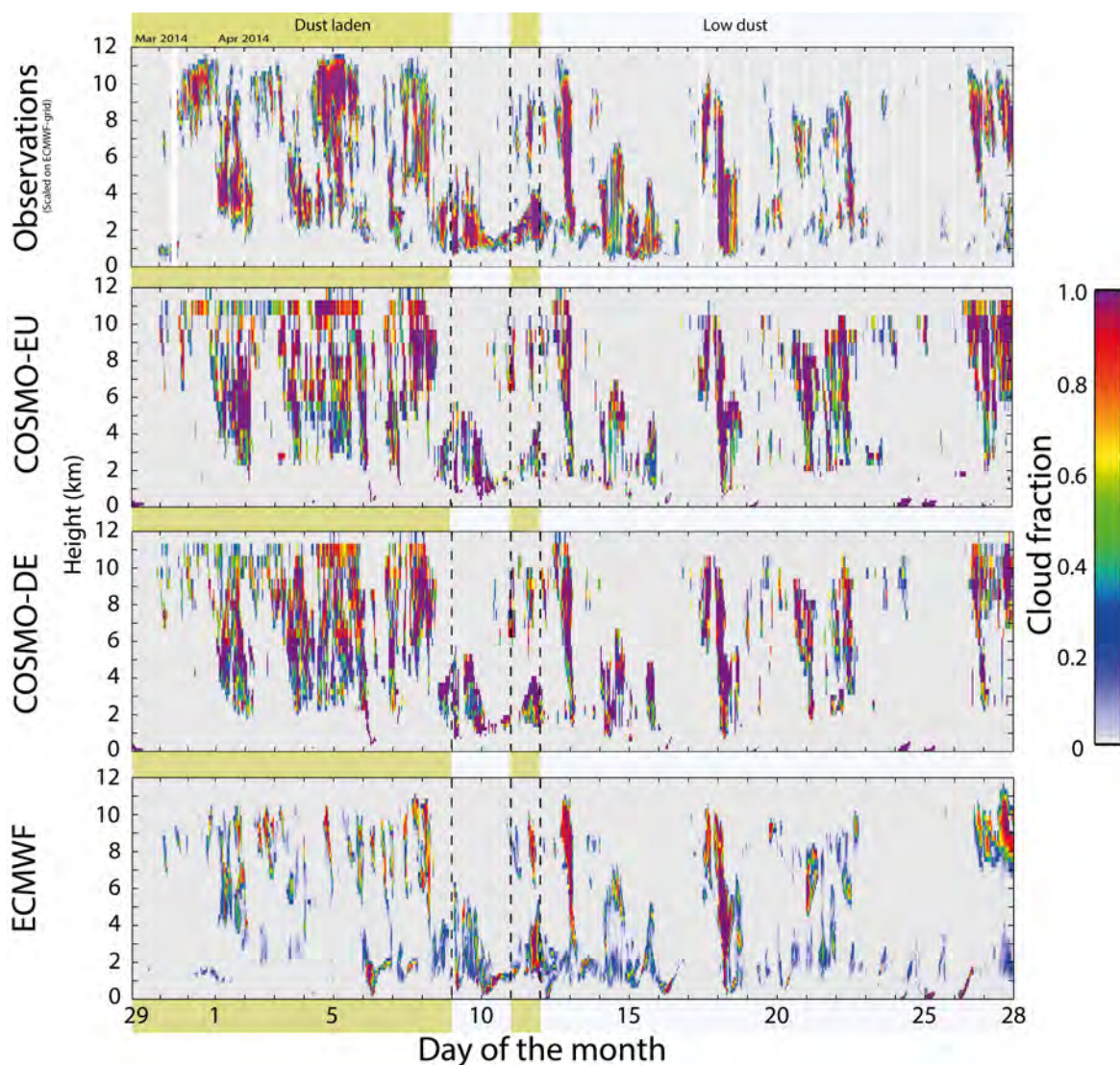


Figure 6.2: Observations and model results for the cloud fraction from the 29th of March until the 28th of April 2014. The top row represents the observations scaled on the ECMWF-IFS model grid. COSMO-EU, COSMO-DE, and ECMWF-IFS forecasts are plotted in the second, third and fourth row, respectively. Days classified as dust-laden are highlighted in ocher and low-dust days in light blue.

the model. The statistical analysis in Figure 6.4a shows a mismatch between model and observations above 2km for dust-laden and 1.5km for low-dust days. Nevertheless the bimodal distribution of the clouds is represented in the model only during the low-dust conditions. COSMO-EU and COMSO-DE show good agreement among themselves and represent the high clouds more precise than ECMWF-IFS. But as seen in Figure 6.4a both models overestimate mid-altitude clouds between 5 and 7km during the dust-laden days. In addition, the bimodal profile of the cloud fraction found by the observations are not captured by any of the models under dust-laden conditions. During the low-dust days the

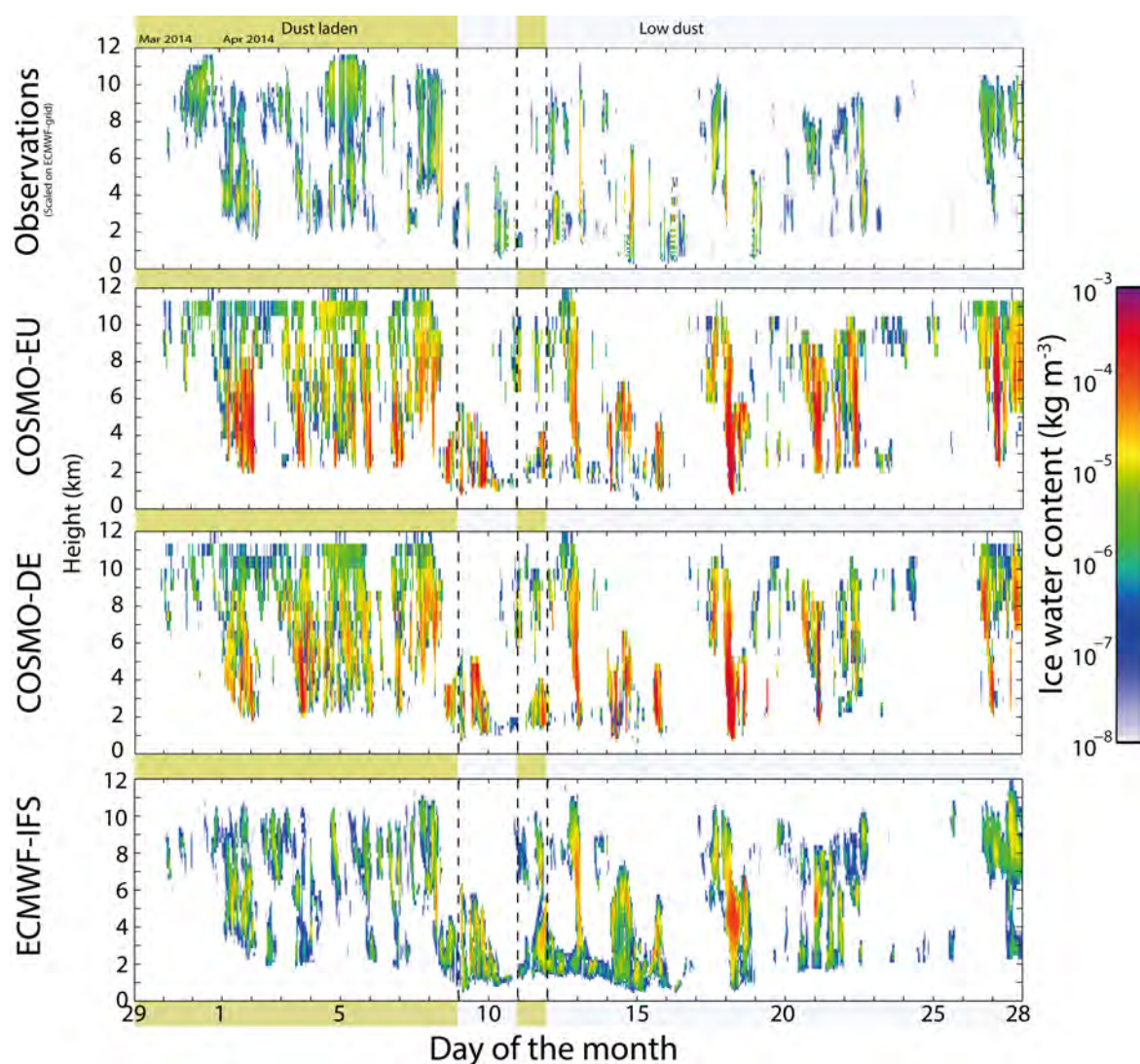


Figure 6.3: Observations and model results for the ice water content from the 29th of March until the 28th of April 2014. The top row represents the observations scaled on the ECMWF-IFS model grid. COSMO-EU, COSMO-DE, and ECMWF-IFS forecasts are plotted in the second, third and fourth row, respectively. Days classified as dust-laden are highlighted in orange and low-dust days in light blue.

agreement between both models and the observations is much better, especially for the COSMO-DE results.

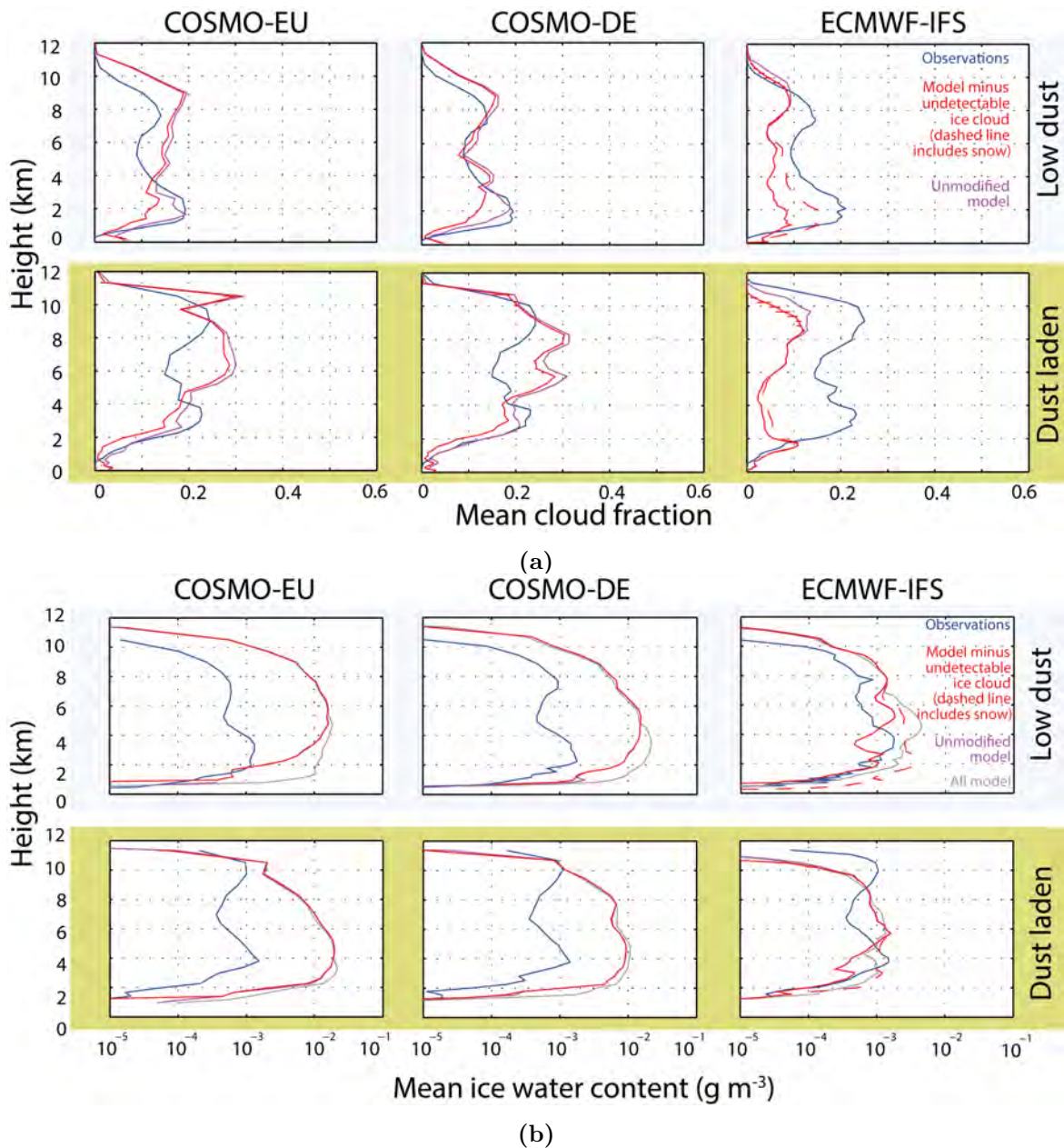


Figure 6.4: (a) represents the statistical analysis of the cloud fraction forecasts from COSMO-EU (left), COSMO-DE (middle) and ECMWF-IFS (right) during the low-dust (top, light blue) and dust-laden days (bottom, ocher). Observations are plotted in blue, while the model results minus undetectable ice clouds are depicted in red (the dashed line in the ECMWF-IFS analysis includes snow). In purple the unmodified model forecasts are represented. (b) shows the same for the IWC.

The ice water content analysis in Figure 6.4b shows an overall quantitative agreement between the observations and the ECMWF-IFS model results. The COSMO-EU or COSMO-DE forecasts on the other hand significantly underestimate the IWC during both periods in the whole column. ECMWF-IFS however slightly overestimates the IWC above 5 km during the low-dust days. Also during the dust-laden days the differences between ECMWF-IFS and observations are not striking but still it fails to reproduce the bimodal distribution seen in the observations. This is, again, also the case for COSMO-EU and COSMO-DE. The discussion of the results will follow in Chapter 8.

Chapter 7

Long-term Statistic

In addition to the case study presented in Chapter 6 a long-term analysis based on the LACROS observations at Leipzig of about two years of COSMO-EU and COSMO-DE data has been done. At the moment of the analysis data from COSMO-EU and COSMO-DE has been available from September 2011 until May 2014, ECMWF-IFS starting from January 2014 and DREAM data was not available after May 2014. Thus to cover as much time as possible the long-term statistic has been limited to COSMO-EU and COSMO-DE. The model results for cloud fraction, IWC and LWC have been evaluated for a period between the first of September 2011 until end of May 2014, if Cloudnet data was available. The data set has been separated according to the dust concentration in four different temperature ranges as described in Section 5.1.2.

The time line of the maximum dust concentration at each day for the four temperature regions during the whole time period is illustrated in Figure 7.1. The critical dust concentration $c_{D_{crit}} = 2 \mu\text{g m}^{-3}$ is marked with a red line and red stars indicate days that have been considered as dust-laden. Dust-free days are marked with green stars whereas black ones indicate days with missing data. For the sake of clarity the lowest value of dust concentration in the plot has been set to $10^{-2} \mu\text{g m}^{-3}$. In Figure 7.1 a general decrease of the maximum daily dust concentration with decreasing temperature (and thus with increasing height) is observable. The most dust-laden days can be found when the dust concentration was analyzed in a temperature range between 0°C and -25°C (just slightly more than for $T > 0^\circ\text{C}$) and the fewest for $T < -40^\circ\text{C}$. The number of days that have been analyzed for each temperature regime and dust concentration are noted in Figures 7.2 – 7.6. Periods where no model evaluation was possible, mainly due to missing observational data, are apparent in Figure 7.1: The first half-year of 2013 (with a short break in March), and September and October 2013, as well as a few shorter periods. During most of these time periods LACROS was either deployed at another site or one of the instruments required for Cloudnet was not available, e.g., because of maintenance. For example in January and February 2013 there was no lidar data available and in March, April, and May as well as in September and October 2013 LACROS was deployed for mea-

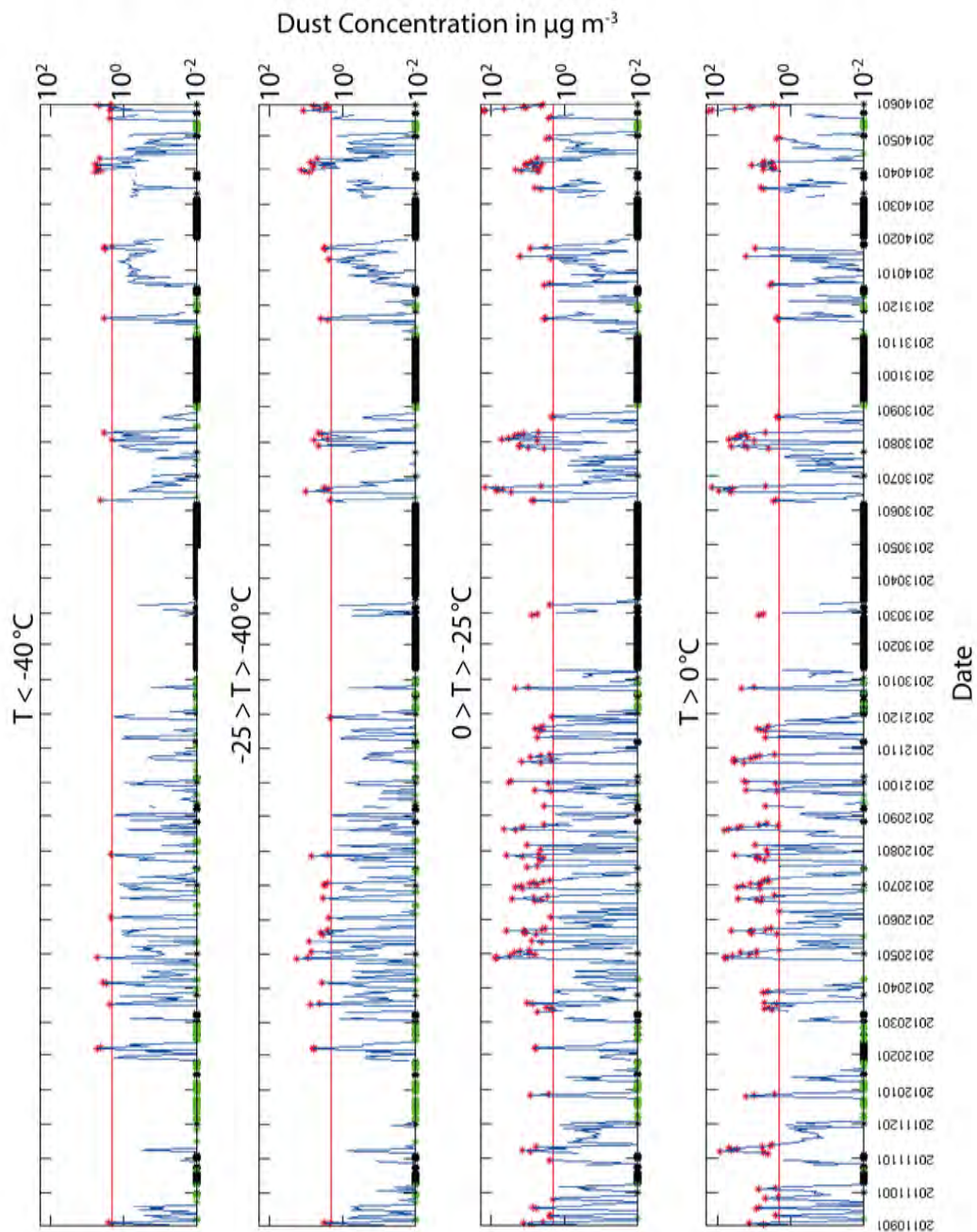


Figure 7.1: Maximum dust concentration during the analyzed time period from September 2011 until June 2014 for the different temperature regimes. The red line indicates the critical dust concentration $c_{D_{crit}} = 2 \mu\text{g m}^{-3}$, dust-laden days are indicated with a red star, dust-free days with a green one. Black stars identify days where no data was available. For the sake of clarity the lowest value of dust concentration in the plot has been set to $10^{-2} \mu\text{g m}^{-3}$.

surement campaigns that took place in Jülich, Germany, and Melpitz, Germany, respectively.

The statistical evaluation of the cloud fraction, ice and liquid water content forecasts in a height between 0 and 12 km of COSMO-EU and COSMO-DE for the long-term analysis is presented in Figures 7.2 - 7.6. The model results have been separated according to their dust concentration into different temperature regimes. The different temperature ranges are plotted next to each other, while the different dust concentrations are plotted on top of each other. In addition the relevant number of days that have been evaluated is specified above each plot. The differing number of analyzed days are due to missing model data. Following the scheme shown in Figure 6.4 the observations are plotted in blue and the model results in red and purple in the Figures 7.3 – 7.5. According to Figure 6.4 red indicates the model results minus undetectable ice clouds and purple the unmodified model.

Figure 7.2 and 7.3 show the evaluation for the cloud fraction from COSMO-EU and COSMO-DE, respectively. Analog to the results shown in Chapter 6 both models show a quite good agreement among each other. Again one can note the higher resolution of

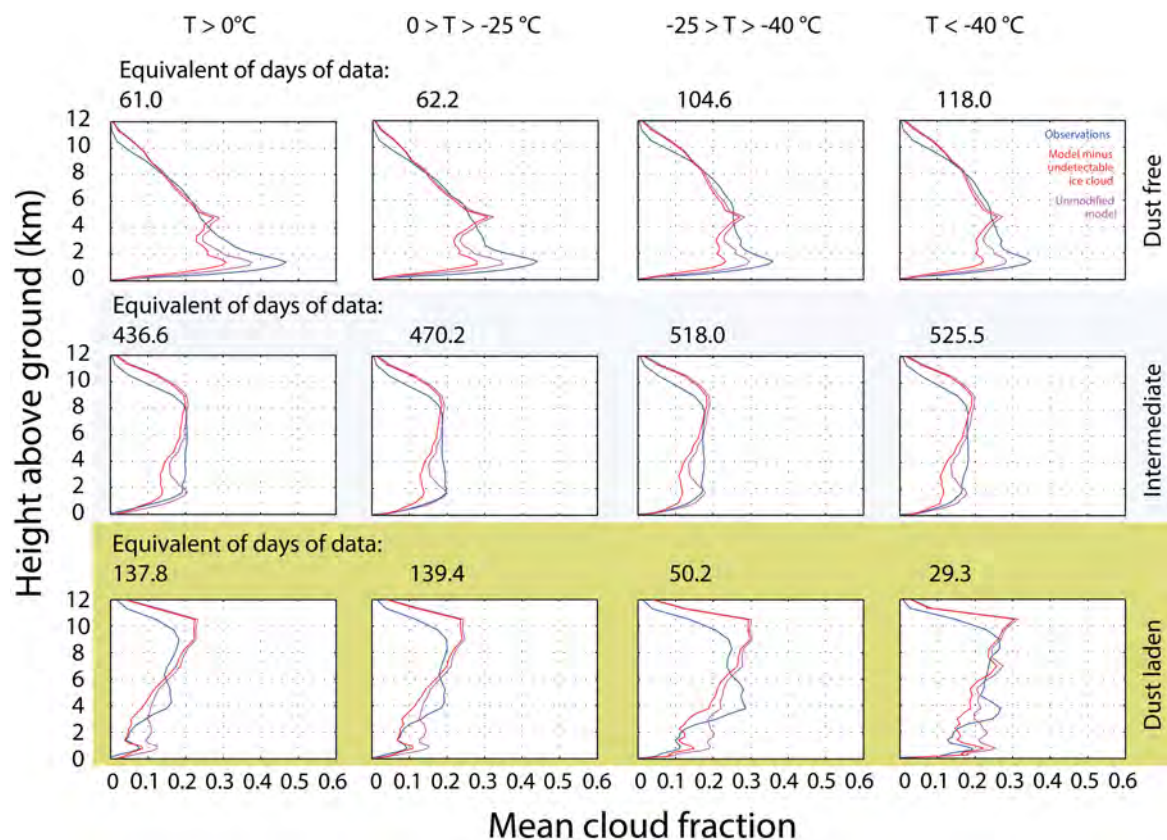


Figure 7.2: Long-term statistical analysis of cloud fraction forecast from COSMO-EU separated by dust concentration (horizontal) in certain temperature ranges (vertical).

COSMO-DE and a slightly better consistency between COSMO-DE and the observations. But both models show a lack of clouds between 3 and 5 km height during the dust-laden days. In contrast to the results in Chapter 6 the mean forecast of the cloud fraction from COSMO-EU and COSMO-DE during the low-dust days show a slightly bimodal cloud distribution with height, which has not been seen by the instruments. During the days considered as dust-free the forecasts are missing partially low clouds between 0 and 2 km. Comparing the observations of the cloud fraction above 6 km a decrease with dust concentration is striking.

In Figure 7.4 and 7.5 the results for the evaluation of ice water content for COSMO-EU and COSMO-DE, respectively, are presented. In this case only a dust concentration separation for a temperature below 0°C has been considered. Partly, differences between both models are distinguishable. While they predict the shape of the IWC distribution with height quite accurate, they have a distinct quantitative overestimation for each dust concentration in any height. For days that have been classified as dust-laden due to their dust concentration found at $T < -40^{\circ}\text{C}$ the observed IWC distribution appears in a bimodal shape. This shape, however, is not visible in the model forecast. Additionally noticeable

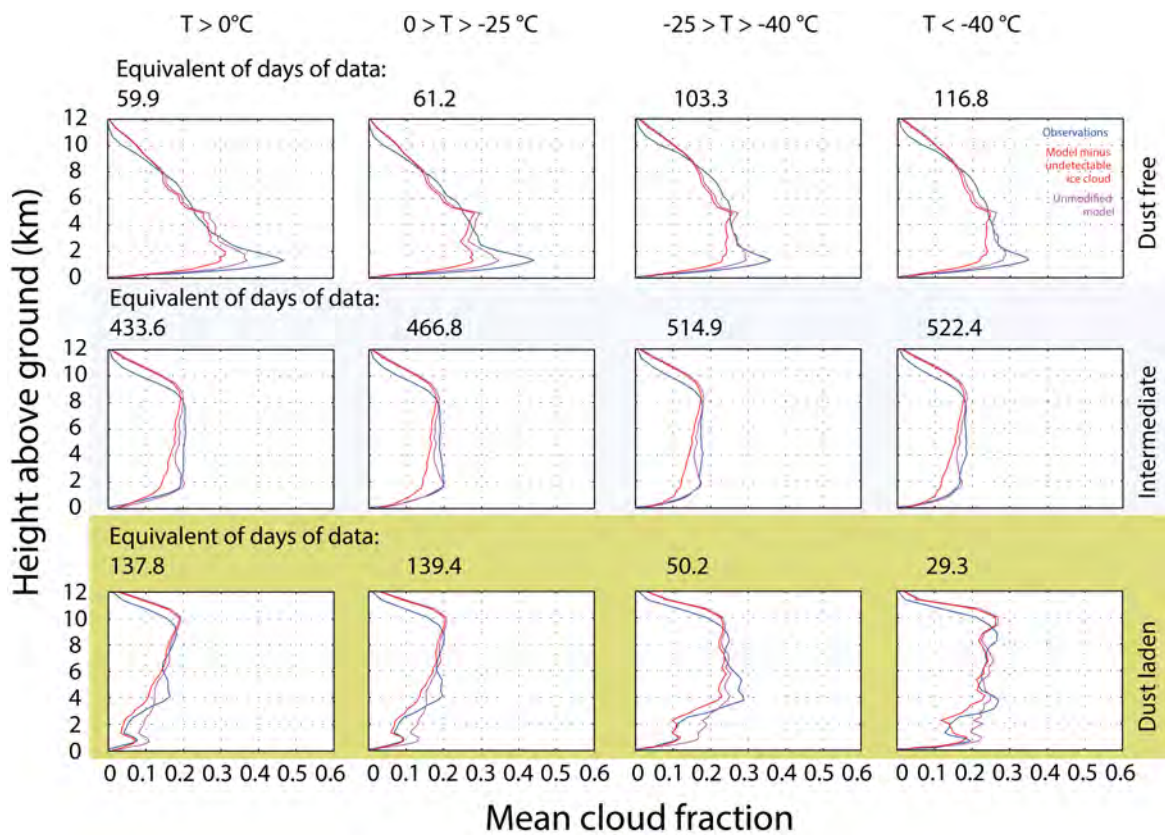


Figure 7.3: Same as 7.2 but for COSMO-DE.

is an increase of IWC observations and forecasts with decreasing dust concentration below 5 km height. Above 6 km altitude on the other hand the IWC increases with increasing dust concentrations.

The analysis for the liquid water content forecast of COSMO-EU and COSMO-DE is shown in Figure 7.6. In red the model results are presented and in blue the Cloudnet observations (the dashed blue line shows the observations assuming a tophat distribution of the adiabatic LWC within the cloud layers). For the COSMO-DE analysis both forecasts and observation show a less smooth graph with more small-scale details but apart from that a similar distribution compared with COMSO-EU. In each dust concentration and temperature range the model LWC reproduces the observed peak around 2 km height quite

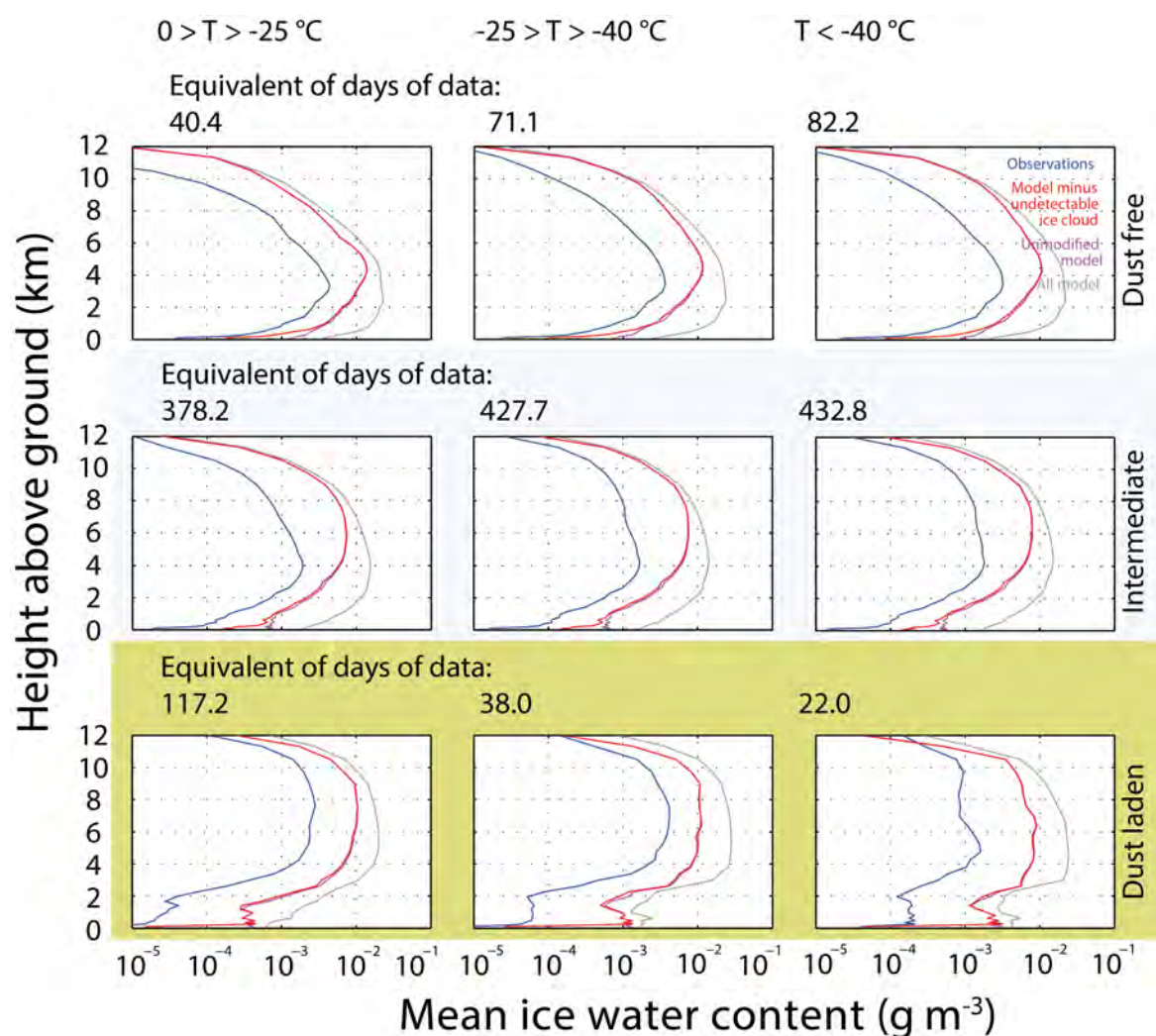


Figure 7.4: Long-term statistical analysis of ice water content forecast from COSMO-EU separated by dust concentration (horizontal) in certain temperature ranges (vertical).

correct but vanishes up to an altitude of less than 5 km. Especially in the analysis of the dust-free and dust-laden days Cloudnet shows a secondary maximum between 5 and 6 km, which is not present in the model results. This secondary maximum loses sharpness when the temperature, at which a high dust concentration was found, decreases. On the other hand it gains sharpness when the temperature, at which no dust was found, decreases. The discussion of the results follows in Chapter 8.

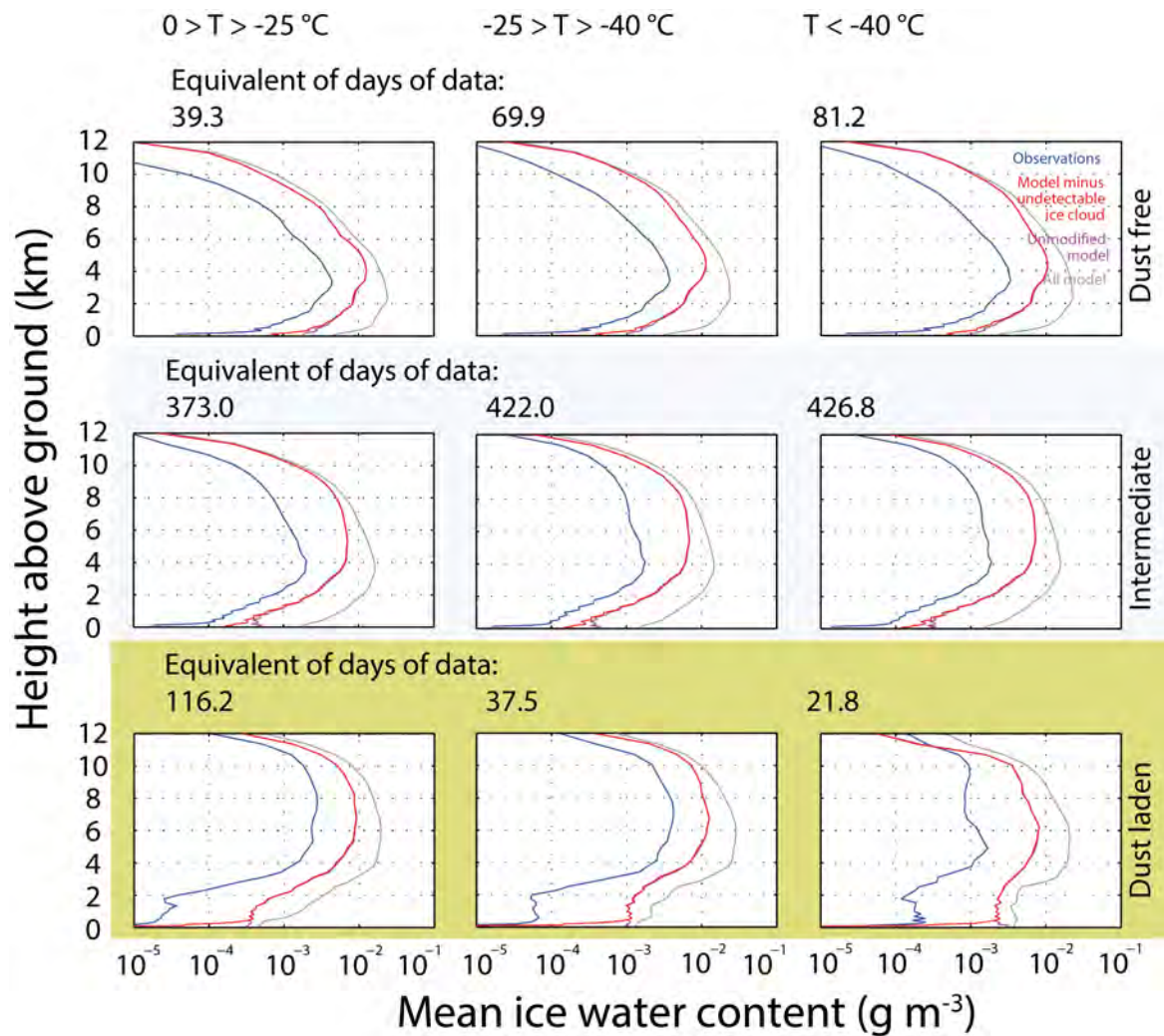


Figure 7.5: Same as Figure 7.4 but for COSMO-DE.

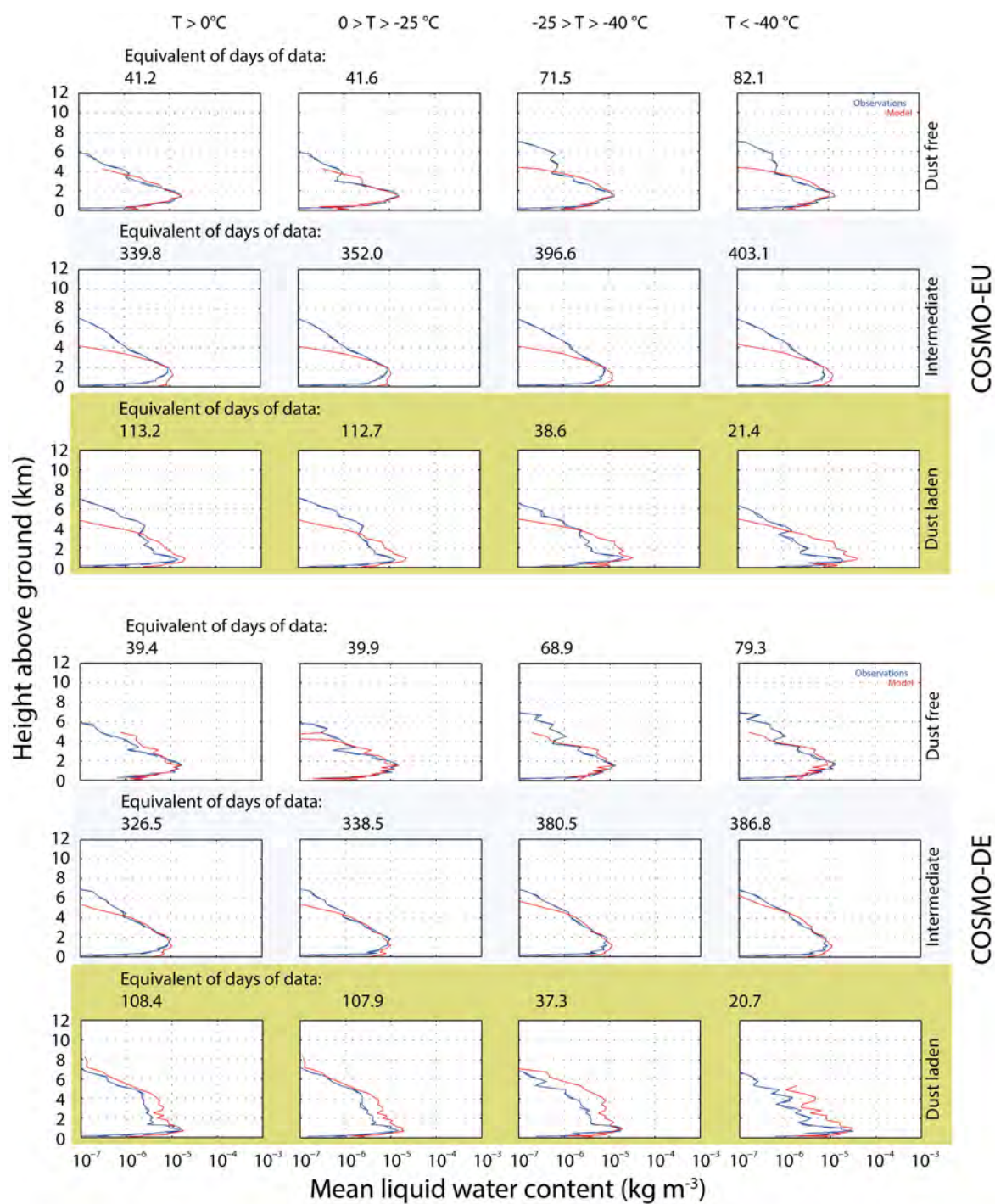


Figure 7.6: Long-term statistical analysis of liquid water content forecast from COSMO-EU (top) and COSMO-DE (bottom) separated by dust concentration (horizontal) in certain temperature ranges (vertical).

Chapter 8

Discussion

Within this Chapter a discussion of the results shown in Chapter 6 and 7 is presented. As reference for the discussion of the case study the observations shown in the top row of Figure 6.2 and 6.3 will be used. During the dust-laden days two distinct long-lasting cirrus layers are visible in the LACROS observations above 8 km height. The first during the 30th and 31st of March and the second on the 4th and 5th of April. The average observed cloud fraction is enhanced during the dust-laden period, which is also visible in the statistical analysis presented in Figure 6.4a (the blue plot represents the observations). In addition a bimodal distribution of both the observed cloud fraction and the observed IWC is obvious during the whole time period. Noticeable is an increase in magnitude and altitude of both peaks of the mean cloud fraction with increasing dust concentration. During the dust-free days the lower peak rises from an altitude of 2 km up to 3 km and from a mean cloud fraction of ~ 0.2 to ~ 0.225 . The upper peak observed at low-dust conditions between 7 and 8 km height with a mean cloud fraction of ~ 0.15 is measured at dust-laden conditions in an altitude of 9 km and with a mean cloud fraction of ~ 0.25 . For the IWC a similar pattern of the bimodal structure is observable but not as distinct as for the cloud fraction. An increased number of CCN and INP due to the high mineral dust concentration can attribute to the enhanced amount of the detected ice and clouds during the dust-laden days.

The two cirrus layers observed at the end of March and begin of April are hardly predicted by any of the three analyzed NWP model forecasts. Both time periods coincidence with a very high dust concentration (cf. Fig. 6.1) and strong vertical mixing. The vertical mixing is already illustrated in Figure 3.4 and is highlighted in Figure 8.1. Presented in Figure 8.1a is a zoom into the vertical velocity observation of the cloud radar between 00:00 and 12:00 UTC on the 5th of April and Figure 8.1b shows the according histogram of the cirrus vertical velocity for the height range from 10 – 11 km and a time range from 02:00 – 05:00 UTC. As can be seen the vertical velocities varied considerable in the range from -4 m s^{-1} to 2.5 m s^{-1} . These vertical movements could have intensified the ice formation because high supersaturations can be reached under such turbulent conditions. Both, homogeneous freezing of solution droplets and heterogeneous ice formation via

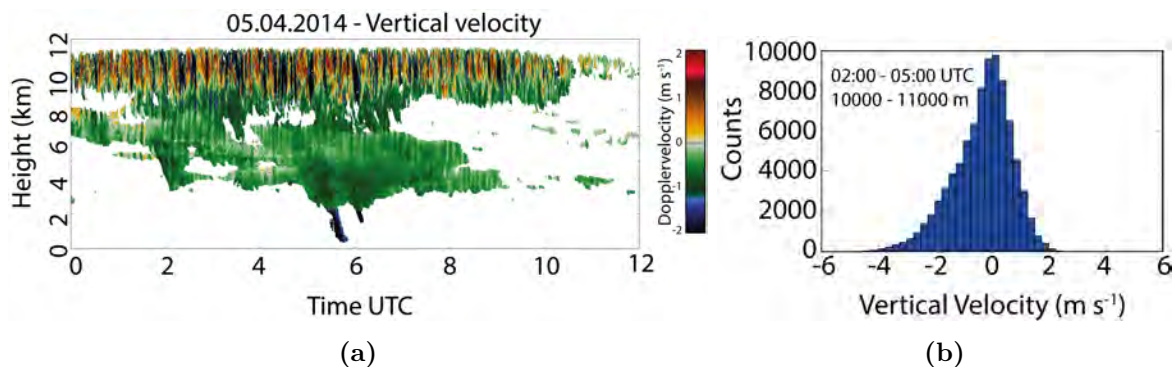


Figure 8.1: Cloud-radar observation of the vertical velocity on 5 April 2014. (a) represents the vertical wind velocity on the 5th of May 2014 between 0:00 and 12:00 UTC. The alternating red and blue shadings indicate a strong mixing with a permanent change of the wind direction. (b) shows the histogram of the velocity of the vertical wind in 10 – 11 km height on the 5th of May 2014 between 2:00 and 5:00 UTC.

the deposition mode are functions of the supersaturation [Kärcher and Lohmann, 2002; Hoose and Möhler, 2012]. Thus, there is a low possibility that the cirrus was induced independently from the dust concentration, just because the turbulence produced high supersaturations. Nevertheless, it should be noted that a change in particle concentration, i.e., INP concentration, is well known to change the relation between ice mass formed homogeneously and heterogeneously, as it was for instance pointed out by Spichtinger and Cziczo [2010]. On the other hand it is also possible that such vertical winds occur more often without being noticed and without having such an influence on the cloud formation, for instance, when much less CCN and INP are present in the upper troposphere.

While COSMO-DE was able to represent the bimodal structure of the cloud fraction during the low-dust days quite accurate the corresponding COSMO-EU results differ evidently, probably due to its lower resolution. The ECMWF-IFS forecasts have determined the structure of the distribution of the cloud fraction during this period but with a distinct underestimation of its magnitude. During the dust-laden days COSMO-EU and COSMO-DE show a strong increase of cloud fraction but not in the adequate altitude. While the observations show the strongest increase between 8 and 10 km height, the model cloud fraction is mainly enhanced between 6 and 8 km height and thus superimposes the bimodal structure. The results of ECMWF-IFS show a slight increase in the magnitude of the upper peak but not in a significant way. The underestimation of cloud fraction during the dust-laden days is rather pronounced.

Comparing the IWC observations in Figure 6.3 to the predicted values by COSMO-EU and COSMO-DE an overestimation of COSMO-EU and COSMO-DE during the whole period especially between 2 and 8 km is obvious. While above all the peak of the observed IWC in higher altitudes is increased in height and magnitude during the dust-laden days

the single peak predicted by both COSMO models is found at lower altitudes for this period. The ice water content forecast by ECMWF-IFS shows a better agreement with the observations. The statistical analysis during the low-dust days in Figure 6.4b does not reveal large differences between model and observations. However the ice inside the cirrus observed at end of March and at the begin of April has not been predicted (cf. Figure 6.3) which probably caused a missing second peak in high altitudes (Fig. 6.4b).

By comparing the mean distribution of the COSMO-EU and COSMO-DE cloud fraction observations for the different dust concentration during the long-term analysis in Figures 7.2 and 7.3 the differences substantiate a reasonable separation. While the dust-free days are characterized by a sharp peak between 1 and 2 km altitude with values for the cloud fraction of about 0.35 – 0.45 followed by a quite smooth decrease starting at 3 km height, the low-dust days show a steep increase of cloud fraction up to 0.2 within the lowest two km which is followed by a nearly constant cloud fraction for the next 6 km and then a decrease to zero in 12 km height. During the dust-laden days a bimodal structure with peaks around 4 and 7 km with values around 0.2 – 0.3 was observed. A general enhancement of cloud fraction with increasing dust concentration especially in higher altitudes and during the days that have been considered as dust-laden at a temperature below -25°C can be seen in the observations. Additionally a bimodal structure in the IWC for days that have been considered as dust-laden at $T < -40^{\circ}\text{C}$ is noticeable. These differences in the vertical structure of the cloud fraction and IWC distribution can be caused by indirect effects induced by the increased INP and CCN concentration due to the high amount of mineral aerosols as described in Section 2.2. But also in this case, semi-direct effects could lead to changes in the thermodynamic structure and consequently in the conditions for cloud formation under dust-laden conditions.

The bimodal structure of the mean cloud fraction during the dust-laden period is not reproduced by both models. COSMO-EU overestimated the cloud fraction in altitudes above 6 km and underestimates it between 3 and 6 km. COSMO-DE, probably again due to its higher resolution, was able to predict the upper peak quite accurate. However it was neither able to predict the lower one.

Another feature can be seen in the LWC analysis when the atmosphere has been categorized as dust-free for $T < -25^{\circ}\text{C}$. The observations show a secondary peak above 4 km that has not been predicted. Due to the missing mineral dust and consequently smaller number of INP it is possible that this increase can be traced back to a reduced formation of ice.

In conclusion, it can be stated that dust-laden conditions lead to the formation of more clouds and more ice. The models, in turn, don't reproduce this behavior. Just from the finding, that mid-level cloud fraction and ice water content increases under dust-laden con-

ditions, points towards an effect of Saharan dust on cloud formation. This could be due to any or a mixture of the possible direct, semi-direct, or indirect effects that were introduced in Chapter 2. For instance, the presence of high dust load can lead to the presence of more CCN and INP, causing the enhanced formation of clouds and ice. But also semi-direct effects, such as modifications of the thermodynamic structure of the atmosphere by the presence of the dust could lead to effects on the cloud properties. A clear answer cannot be given in the scope of this study.

Chapter 9

Conclusion and Outlook

Within the presented study, the impact of mineral dust on the predictability of cloud properties by NWP models has been studied. To the knowledge of the author this is the first long-time evaluation of the effect of mineral dust on the forecast quality of numerical weather prediction models in terms of the vertical distribution of cloud properties. In doing so, cloud fraction, ice water content, and liquid water content forecasts have been analyzed during time episodes characterized by three different dust concentrations: dust-free ones with a dust-concentration of $c_D = 0 \mu\text{g m}^{-3}$, dust-laden ones with a dust concentration exceeding $c_{D_{crit}} = 2 \mu\text{g m}^{-3}$, and intermediate ones. Time periods with a high, low, and zero dust pollution have been identified by the atmospheric dust forecast system DREAM in different temperature regimes and their analyses have been compared to each other. Model results provided by the NWP models COSMO-EU, COSMO-DE, and ECMWF-IFS have been statistically evaluated during and shortly after a dust outbreak at Leipzig in spring 2014. In addition a long-term evaluation for a two year data set between September 2011 and June 2014 of COSMO-EU and COSMO-DE forecasts for Leipzig has been made. The model data has been compared to observational data provided by the remote sensing super site LACROS at TROPOS in Leipzig and evaluated using Cloudnet algorithms and first results have already been presented on the DUST 2016 conference [*Griesche et al.*, 2016]. Additionally an incorporation of the regional model system COSMO-MUSCAT, which is based on the nonhydrostatic model COSMO and the online-coupled 3-D chemistry tracer transport model MultiScale Chemistry Aerosol Transport Model (MUSCAT) [*Heinold et al.*, 2011b], has been anticipated. But due to delays based on essential reruns of the model an integration of these results was not possible within the designated time period for this study.

Disagreements have been found in between the different model predictions, especially during the case study between ECMWF-IFS and COSMO-EU as well as COSMO-DE (Fig. 6.2). The differences between COMSO-EU and COSMO-DE have not been that distinct, neither during the case study nor during the long-term study. Nevertheless both, the April-2014 and the long-term studies, revealed disagreements between the observations and

results of all three models. In both cases the best agreements have been found during the low-dust days, i.e., under conditions with intermediate dust conditions (Fig. 7.2, 7.3, 7.4, 7.5 and 7.6). As has been noted in Chapter 4, the aerosol parameterization in all three investigated models are based on mean values given in *Tegen et al.* [1997], which to a certain extent can explain that models and observations agree best under intermediate conditions.

This study has determined the difficulty of separating direct, semi-direct, and indirect effects of the desert dust in NWP model results. Direct and semi-direct effects can modify the thermodynamic structure of the atmosphere [*Tegen and Lacis*, 1996; *Seinfeld et al.*, 1998; *Ackerman et al.*, 2000; *Miller et al.*, 2006; *Koch and Del Genio*, 2010; *Heinold et al.*, 2011b; *Choobari et al.*, 2014] and thus clouds may have formed differently or at different places. Indications of that can be seen in Figures 6.2, 6.4a, 7.2, and 7.3. An influence of mineral dust on the vertical structure of the cloud fraction is obvious as well as a significant improved agreement during the low-dust days between model and LACROS results and a degradation of the model performance during the dust-laden days.

Next steps to continue and deepen this approach could be to include the ECMWF-IFS forecasts in the long-term study and provide the statistics as a function of temperature instead of a function of height. Also different forecast time periods can be analyzed. In this study the 3 – 5 hours forecast of COSMO-EU and COSMO-DE has been used as well as the 12 – 35 hours forecast of ECMWF-IFS. If a degradation of forecast skills with forecast time period can be determined this suggests an insufficient representation of processes that can be associated with mineral dust. Additionally an extension of the analysis to models that incorporate aerosol properties and their interaction with the radiative transfer and cloud microphysics such as COSMO-MUSCAT should be aspired. COSMO-MUSCAT has already been used by *Heinold et al.* [2011a] to analyze the radiative forcing by Saharan Dust and biomass-burning aerosol. Future studies should also show under which conditions cirrus clouds form under turbulent conditions as shown in Figure 8.1. If this is a distinct feature of dust-laden episodes, it is likely that the dust plays a major role in the formation of ice crystals at such conditions. The investigation of the cirrus formation under turbulent, dust-laden conditions will in addition require higher resolved model simulation which can thoroughly capture the strong variability of the vertical air motion.

Bibliography

- Abbe, C. (1901), The Physical Basis of Long-Range Weather FORECASTS¹, *Monthly Weather Review*, *29*, 551, doi:10.1175/1520-0493(1901)29[551c:TPBOLW]2.0.CO;2.
- Ackerman, A. S., O. B. Toon, D. E. Stevens, A. J. Heymsfield, V. Ramanathan, and E. J. Welton (2000), Reduction of tropical cloudiness by soot, *Science*, *288*, 1042-1047, doi:10.1126/science.288.5468.1042.
- Albrecht, B. A. (1989), Aerosols, cloud microphysics, and fractional cloudiness, *Science*, *245*, 1227-1230, doi:10.1126/science.245.4923.1227.
- Albrecht, B. A., C. W. Fairall, D. W. Thomson, A. B. White, J. B. Snider, and W. H. Schubert (1990), Surface-based remote sensing of the observed and the Adiabatic liquid water content of stratocumulus clouds, *Geophysical Research Letters*, *17*, 89-92, doi:10.1029/GL017i001p00089.
- Ansmann, A., M. Riebesell, and C. Weitkamp (1990), Measurement of atmospheric aerosol extinction profiles with a Raman lidar, *Optics Letters*, *15*, 746-748, doi:10.1364/OL.15.000746.
- Ansmann, A., M. Tesche, P. Seifert, D. Althausen, R. Engelmann, J. Fruntke, U. Wandinger, I. Mattis, and D. Müller (2009), Evolution of the ice phase in tropical altocumulus: SAMUM lidar observations over Cape Verde, *Journal of Geophysical Research (Atmospheres)*, *114* (D17), D17208, doi:10.1029/2008JD011659.
- Atkins, P., and J. de Paula (2002), *Atkins' Physical Chemistry*, 7 ed., Oxford.
- Baldauf, M., S. Förstner, S. Klink, T. Reinhardt, C. Schraff, A. Seifert, and K. Stephan (2014), Kurze Beschreibung des Lokal-Modells Kürzestfrist COSMO-DE (LMK) und seiner Datenbanken auf dem Datenserver des DWD, *Deutscher Wetterdienst*.
- Bangert, M., A. Nenes, B. Vogel, H. Vogel, D. Barahona, V. A. Karydis, P. Kumar, C. Kottmeier, and U. Blahak (2012), Saharan dust event impacts on cloud formation and radiation over Western Europe, *Atmospheric Chemistry & Physics*, *12*, 4045-4063, doi:10.5194/acp-12-4045-2012.
-

- Basart, S., C. Pérez, S. Nickovic, E. Cuevas, and J. Baldasano (2012), Development and evaluation of the BSC-DREAM8b dust regional model over Northern Africa, the Mediterranean and the Middle East, *Tellus B*, *64*(0).
- Bauer, P., A. Thorpe, and G. Brunet (2015), The quiet revolution of numerical weather prediction, *Nature*, *525*, 47-55, doi:10.1038/nature14956.
- Bjerknes, V. (1904), Das Problem der Wettervorhersage, betrachtet vom Standpunkte der Mechanik und der Physik, *Meteorologische Zeitschrift*.
- Borrego, C., and S. Incecik (Eds.) (2004), *Air pollution modeling and its application XVI*, chap. The chemistry-transport modeling system LM-MUSCAT: Description and CityDelta applications, pp. 427–439, Springer US, Boston, MA, doi:10.1007/978-1-4419-8867-6_39.
- Bouniol, D., A. Protat, J. Delanoë, J. Pelon, J.-M. Piriou, F. Bouyssel, A. M. Tompkins, D. R. Wilson, Y. Morille, M. Haeffelin, E. J. O'Connor, R. J. Hogan, A. J. Illingworth, D. P. Donovan, and H.-K. Baltink (2010), Using continuous ground-based radar and lidar measurements for evaluating the representation of clouds in four operational models, *Journal of Applied Meteorology and Climatology*, *49*, 1971-1991, doi:10.1175/2010JAMC2333.1.
- Bühl, J., P. Seifert, A. Myagkov, and A. Ansmann (2016), Relation between ice and liquid water mass in mixed-phase cloud layers measured with Cloudnet, *Atmospheric Chemistry & Physics Discussions*, *2016*, 1–19, doi:10.5194/acp-2016-25.
- Choobari, O. A., P. Zawar-Reza, and A. Sturman (2014), The global distribution of mineral dust and its impacts on the climate system: A review, *Atmospheric Research*, *138*, 152-165, doi:10.1016/j.atmosres.2013.11.007.
- Chung, S. H., and J. H. Seinfeld (2002), Global distribution and climate forcing of carbonaceous aerosols, *Journal of Geophysical Research: Atmospheres*, *107*(D19), AAC 14-1–AAC 14-33, doi:10.1029/2001JD001397, 4407.
- Cloudnet (2016), Cloudnet measurements, <http://lacros.rsd.tropos.de/cloudnet/cloudnet.php>.
- Crewell, S., U. Lhnert, M. Mech, and C. Simmer (2011), Mikrowellenradiometrie für Wasserdampf- und Wolkenbeobachtung (Microwave radiometry for water cloud observations), *Promet*, *36*(3/4), 109-118.
- de Boer, G., H. Morrison, M. D. Shupe, and R. Hildner (2011), Evidence of liquid dependent ice nucleation in high-latitude stratiform clouds from surface remote sensors, *Geophysical Research Letters*, *38*, L01803, doi:10.1029/2010GL046016.
- Doms, G., and M. Baldauf (2015), A Description of the Nonhydrostatic Regional COSMO-Model - Part I: Dynamics and Numerics, *Deutscher Wetterdienst*.
- DREAM (2015), BSC-DREAM8b v2.0, <http://www.bsc.es/earth-sciences/mineral-dust/catalogo-datos-dust>.
-

- ECMWF (2016), IFS documentation, <http://www.ecmwf.int/en/forecasts/documentation-and-support/changes-ecmwf-model/ifs-documentation>.
- Flentje, H., B. Briel, C. Beck, M. Collaud Coen, M. Fricke, J. Cyrus, J. Gu, M. Pitz, and W. Thomas (2015), Identification and monitoring of Saharan dust: An inventory representative for south Germany since 1997, *Atmospheric Environment*, *109*, 87-96, doi:10.1016/j.atmosenv.2015.02.023.
- Frisch, A. S., C. W. Fairall, and J. B. Snider (1995), Measurement of stratus cloud and drizzle parameters in ASTEX with a K_{α} -band Doppler radar and a microwave radiometer., *Journal of Atmospheric Sciences*, *52*, 2788-2799, doi:10.1175/1520-0469(1995)052<2788:MOSCAD>2.0.CO;2.
- Griesche, H., P. Seifert, I. Tegen, and B. Heinold (2016), Exploiting remote sensing observations to evaluate the effect of dust aerosol on the forecast skill of numerical weather prediction models, in *DUST 2016*.
- Grzeschik, M., H.-S. Bauer, V. Wulfmeyer, D. Engelbart, U. Wandinger, I. Mattis, D. Althausen, R. Engelmann, M. Tesche, and A. Riede (2008), Four-dimensional variational data analysis of water vapor Raman lidar data and their impact on mesoscale forecasts, *Journal of Atmospheric and Oceanic Technology*, *25*, 1437, doi:10.1175/2007JTECHA974.1.
- Gunn, K. L. S., and J. S. Marshall (1958), The distribution with size of aggregate snowflakes., *Journal of Atmospheric Sciences*, *15*, 452-461, doi:10.1175/1520-0469(1958)015<0452:TDWSOA>2.0.CO;2.
- Hansen, J., M. Sato, and R. Ruedy (1997), Radiative forcing and climate response, *Journal of Geophysical Research (Atmospheres)*, *102*, 6831-6864, doi:10.1029/96JD03436.
- Heinold, B., I. Tegen, S. Bauer, and M. Wendisch (2011a), Regional modelling of Saharan dust and biomass-burning smoke. Part 2: Direct radiative forcing and atmospheric dynamic response, *Tellus Series B Chemical and Physical Meteorology B*, *63*, 800-813, doi:10.1111/j.1600-0889.2011.00574.x.
- Heinold, B., I. Tegen, K. Schepanski, M. Tesche, M. Esselborn, V. Freudenthaler, S. Gross, K. Kandler, P. Knippertz, D. Müller, A. Schladitz, C. Toledano, B. Weinzierl, A. Ansmann, D. Althausen, T. Müller, A. Petzold, and A. Wiedensohler (2011b), Regional modelling of Saharan dust and biomass-burning smoke. Part I: Model description and evaluation, *Tellus Series B Chemical and Physical Meteorology B*, *63*, 781-799, doi:10.1111/j.1600-0889.2011.00570.x.
- Heintzenberg, J. (2009), The SAMUM-1 experiment over Southern Morocco: overview and introduction, *Tellus Series B Chemical and Physical Meteorology B*, *61*, 2-11, doi:10.1111/j.1600-0889.2008.00403.x.
-

- Hogan, R. J., and A. J. Illingworth (2003), Parameterizing ice cloud inhomogeneity and the overlap of inhomogeneities using cloud radar data, in *EGS - AGU - EUG Joint Assembly*.
- Hogan, R. J., C. Jakob, and A. J. Illingworth (2001), Comparison of ECMWF winter-season cloud fraction with radar-derived values., *Journal of Applied Meteorology*, *40*, 513-525, doi:10.1175/1520-0450(2001)040<0513:COEWSC>2.0.CO;2.
- Hogan, R. J., M. P. Mittermaier, and A. J. Illingworth (2006), The retrieval of ice water content from radar reflectivity factor and temperature and its use in evaluating a mesoscale model, *Journal of Applied Meteorology and Climatology*, *45*, 301-317, doi:10.1175/JAM2340.1.
- Hoose, C., and O. Möhler (2012), Heterogeneous ice nucleation on atmospheric aerosols: a review of results from laboratory experiments, *Atmospheric Chemistry & Physics*, *12*, 9817-9854, doi:10.5194/acp-12-9817-2012.
- Illingworth, A. J., R. J. Hogan, E. J. O'Connor, D. Bouniol, M. E. Brooks, J. Delanoë, D. P. Donovan, J. D. Eastment, N. Gaussiat, J. W. F. Goddard, M. Haefelin, H. K. Baltink, O. A. Krasnov, J. Pelon, J.-M. Piriou, A. Protat, H. W. J. Russchenberg, A. Seifert, A. M. Tompkins, G.-J. van Zadelhoff, F. Vinit, U. Willén, D. R. Wilson, and C. L. Wrench (2007), Cloudnet, *Bulletin of the American Meteorological Society*, *88*, 883, doi:10.1175/BAMS-88-6-883.
- Jickells, T. D., Z. S. An, K. K. Andersen, A. R. Baker, G. Bergametti, N. Brooks, J. J. Cao, P. W. Boyd, R. A. Duce, K. A. Hunter, H. Kawahata, N. Kubilay, J. laRoche, P. S. Liss, N. Mahowald, J. M. Prospero, A. J. Ridgwell, I. Tegen, and R. Torres (2005), Global iron connections between desert dust, ocean biogeochemistry, and climate, *Science*, *308*, 67-71, doi:10.1126/science.1105959.
- Kärcher, B., and U. Lohmann (2002), A parameterization of cirrus cloud formation: Homogeneous freezing including effects of aerosol size, *Journal of Geophysical Research: Atmospheres*, *107*(D23), AAC 9-1–AAC 9-10, doi:10.1029/2001JD001429, 4698.
- Koch, D., and A. D. Del Genio (2010), Black carbon semi-direct effects on cloud cover: review and synthesis, *Atmospheric Chemistry & Physics*, *10*, 7685-7696.
- Köhler, H. (1936), The nucleus in and the growth of hygroscopic droplets, *Trans. Faraday Soc.*, *32*, 1152-1161, doi:10.1039/TF9363201152.
- Laurent, B., B. Marticorena, G. Bergametti, J. F. Lon, and N. M. Mahowald (2008), Modeling mineral dust emissions from the Sahara desert using new surface properties and soil database, *Journal of Geophysical Research: Atmospheres*, *113*(D14), n/a–n/a, doi:10.1029/2007JD009484, d14218.
- Levin, Z., A. Teller, E. Ganor, and Y. Yin (2005), On the interactions of mineral dust, sea-salt particles, and clouds: A measurement and modeling study from the Mediterranean Israeli
-

- Dust Experiment campaign, *Journal of Geophysical Research (Atmospheres)*, 110(D20), D20202, doi:10.1029/2005JD005810.
- Li, F., A. M. Vogelmann, and V. Ramanathan (2004), Saharan dust aerosol radiative forcing measured from space., *Journal of Climate*, 17, 2558-2571, doi:10.1175/1520-0442(2004)017<2558:SDARFM>2.0.CO;2.
- Mace, G. G., C. Jakob, and K. P. Moran (1998), Validation of hydrometeor occurrence predicted by the ECMWF Model using millimeter wave radar data, *Geophysical Research Letters*, 25, 1645-1648, doi:10.1029/98GL00845.
- Marshall, J. S., and W. M. K. Palmer (1948), The distribution of rainsdrops with size, *Journal of Meteorology*, 5(4), 165-166, doi:10.1175/1520-0469(1948)005<0165:TDORWS>2.0.CO;2.
- McCormick, R. A., and J. H. Ludwig (1967), Climate modification by atmospheric aerosols, *Science*, 156, 1358-1359, doi:10.1126/science.156.3780.1358.
- Merk, D., H. Deneke, B. Pospichal, and P. Seifert (2016), Investigation of the adiabatic assumption for estimating cloud micro- and macrophysical properties from satellite and ground observations, *Atmospheric Chemistry & Physics*, 16(2), 933-952, doi:10.5194/acp-16-933-2016.
- Miles, N. L., J. Verlinde, and E. E. Clothiaux (2000), Cloud droplet size distributions in low-level stratiform clouds., *Journal of Atmospheric Sciences*, 57, 295-311, doi:10.1175/1520-0469(2000)057<0295:CDS DIL>2.0.CO;2.
- Miller, R. L., and I. Tegen (1998), Climate Response to Soil Dust Aerosols., *Journal of Climate*, 11, 3247-3267, doi:10.1175/1520-0442(1998)011<3247:CRTSDA>2.0.CO;2.
- Miller, R. L., R. V. Cakmur, J. Perlwitz, I. V. Geogdzhayev, P. Ginoux, D. Koch, K. E. Kohfeld, C. Prigent, R. Ruedy, G. A. Schmidt, and I. Tegen (2006), Mineral dust aerosols in the NASA Goddard Institute for Space Sciences ModelE atmospheric general circulation model, *Journal of Geophysical Research (Atmospheres)*, 111, D06208, doi:10.1029/2005JD005796.
- Orikasa, N., M. Murakami, and A. J. Heymsfield (2013), Ice crystal concentration in midlatitude cirrus clouds: In situ measurements with the balloonborne hydrometeor videonde (HYVIS), *Journal of the Meteorological Society of Japan. Ser. I*, 91(2), 143-161, doi:10.2151/jmsj.2013-204.
- Painter, T. H., A. P. Barrett, C. C. Landry, J. C. Neff, M. P. Cassidy, C. R. Lawrence, K. E. McBride, and G. L. Farmer (2007), Impact of disturbed desert soils on duration of mountain snow cover, *Geophysical Research Letters*, 34, L12502, doi:10.1029/2007GL030284.
-

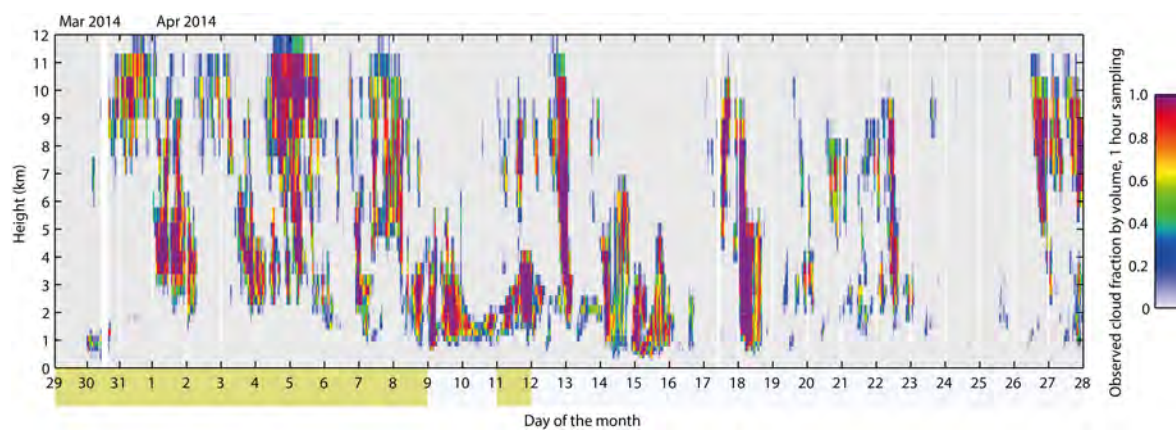
- Pérez, C., S. Nickovic, J. M. Baldasano, M. Sicard, F. Rocadenbosch, and V. E. Cachorro (2006a), A long Saharan dust event over the western Mediterranean: Lidar, Sun photometer observations, and regional dust modeling, *Journal of Geophysical Research (Atmospheres)*, *111*(D15), D15214, doi:10.1029/2005JD006579.
- Pérez, C., S. Nickovic, G. Pejanovic, J. M. Baldasano, and E. Ñ-Zsoy (2006b), Interactive dust-radiation modeling: A step to improve weather forecasts, *Journal of Geophysical Research (Atmospheres)*, *111*(D16), D16206, doi:10.1029/2005JD006717.
- Peters, G., and U. Görzdorf (2011), Wolkenradar — Prinzipien und Messungen (Cloudradar — Fundamentals and Measurements), *Promet*, *36*(3/4), 144-153.
- Pope, C. A., R. T. Burnett, M. J. Thun, E. E. Calle, D. Krewski, K. Ito, and G. D. Thurston (2002), Lung cancer, cardiopulmonary mortality, and long-term exposure to fine particulate air pollution., *JAMA*, *287*(9), 1132-1141, doi:10.1001/jama.287.9.1132.
- Prospero, J., P. Ginoux, O. Torres, S. Nicholson, and T. Gill (2002), Environmental characterization of global sources of atmospheric soil dust identified with the Nimbus 7 Total Ozone Mapping Spectrometer (TOMS) absorbing aerosol product, *Reviews of Geophysics*, *40*(1).
- Prospero, J. M. (1999), Long-term measurements of the transport of African mineral dust to the southeastern United States: Implications for regional air quality, *Journal of Geophysical Research: Atmospheres*, *104*, 15, doi:10.1029/1999JD900072.
- Pruppacher, H., and J. Klett (2010), *Microphysics of clouds and precipitation*, Atmospheric and Oceanographic Sciences Library, Springer Netherlands.
- Rosenfeld, D., Y. Rudich, and R. Lahav (2001), Desert dust suppressing precipitation: a possible desertification feedback loop, *Proceedings of the National Academy of Science*, *98*, 5975-5980, doi:10.1073/pnas.101122798.
- Sassen, K. (1984), Deep orographic cloud structure and composition derived from comprehensive remote sensing measurements., *Journal of Applied Meteorology*, *23*, 568-583, doi:10.1175/1520-0450(1984)023<0568:DOCSAC>2.0.CO;2.
- Sassen, K., P. J. DeMott, J. M. Prospero, and M. R. Poellot (2003), Saharan dust storms and indirect aerosol effects on clouds: CRYSTAL-FACE results, *Geophysical Research Letters*, *30*, 1633, doi:10.1029/2003GL017371.
- Schättler, U., and U. Blahak (2015), A description of the nonhydrostatic regional COSMO-Model Part V: Preprocessing: Initial and boundary data for the COSMO-Model, *Deutscher Wetterdienst*.
- Schulz, J.-P., and U. Schättler (2014), Kurze Beschreibung des Lokal-Modells Europa COSMO-EU (LME) und seiner Datenbanken auf dem Datenserver des DWD, *Deutscher Wetterdienst*.
-

- Seifert, P., A. Ansmann, I. Mattis, U. Wandinger, M. Tesche, R. Engelmann, D. Müller, C. Pérez, and K. Haustein (2010), Saharan dust and heterogeneous ice formation: Eleven years of cloud observations at a central European EARLINET site, *Journal of Geophysical Research (Atmospheres)*, 115(D20), D20201, doi:10.1029/2009JD013222.
- Seinfeld, J. H., S. N. Pandis, and K. Noone (1998), Atmospheric chemistry and physics: From air pollution to climate change, *Physics Today*, 51, 88, doi:10.1063/1.882420.
- Shupe, M. D. (2007), A ground-based multisensor cloud phase classifier, *Geophysical Research Letters*, 34, L22809, doi:10.1029/2007GL031008.
- Solomon, S., D. Qin, M. Manning, Z. Chen, M. Marquis, K. B. Averyt, M. Tignor, and H. L. Miller (Eds.) (2007), *Climate change 2007 - The physical science basis: Working group I contribution to the fourth assessment report of the IPCC*, Cambridge University Press.
- Spichtinger, P., and D. J. Cziczo (2010), Impact of heterogeneous ice nuclei on homogeneous freezing events in cirrus clouds, *Journal of Geophysical Research: Atmospheres*, 115(D14), n/a–n/a, doi:10.1029/2009JD012168, d14208.
- Steppler, J., G. Doms, U. Schättler, H. W. Bitzer, A. Gassmann, U. Damrath, and G. Gregoric (2003), Meso-gamma scale forecasts using the nonhydrostatic model LM, *Meteorology and Atmospheric Physics*, 82, 75-96, doi:10.1007/s00703-001-0592-9.
- Stocker, T., D. Qin, G.-K. Plattner, M. Tignor, S. Allen, J. Boschung, A. Nauels, Y. Xia, V. Bex, and P. Midgley (Eds.) (2013), *Climate Change 2013 - The Physical Science Basis: Contribution of Working Group I to the Fifth Assessment Report of the Intergovernmental Panel on Climate Change*, Cambridge University Press, Cambridge, United Kingdom and New York, NY, USA, doi:10.1017/CBO9781107415324.018.
- Targino, A. C., R. Krejci, K. J. Noone, and P. Glantz (2006), Single particle analysis of ice crystal residuals observed in orographic wave clouds over Scandinavia during INTACC experiment, *Atmospheric Chemistry & Physics*, 6, 1977-1990.
- Tegen, I., and A. A. Lacis (1996), Modeling of particle size distribution and its influence on the radiative properties of mineral dust aerosol, *Journal of Geophysical Research: Atmospheres*, 101(D14), 19237–19244, doi:10.1029/95JD03610.
- Tegen, I., P. Hollrig, M. Chin, I. Fung, D. Jacob, and J. Penner (1997), Contribution of different aerosol species to the global aerosol extinction optical thickness: Estimates from model results, *Journal of Geophysical Research: Atmospheres*, 102, 23, doi:10.1029/97JD01864.
- Teller, A., and Z. Levin (2006), The effects of aerosols on precipitation and dimensions of subtropical clouds: a sensitivity study using a numerical cloud model, *Atmospheric Chemistry & Physics*, 6, 67-80.
-

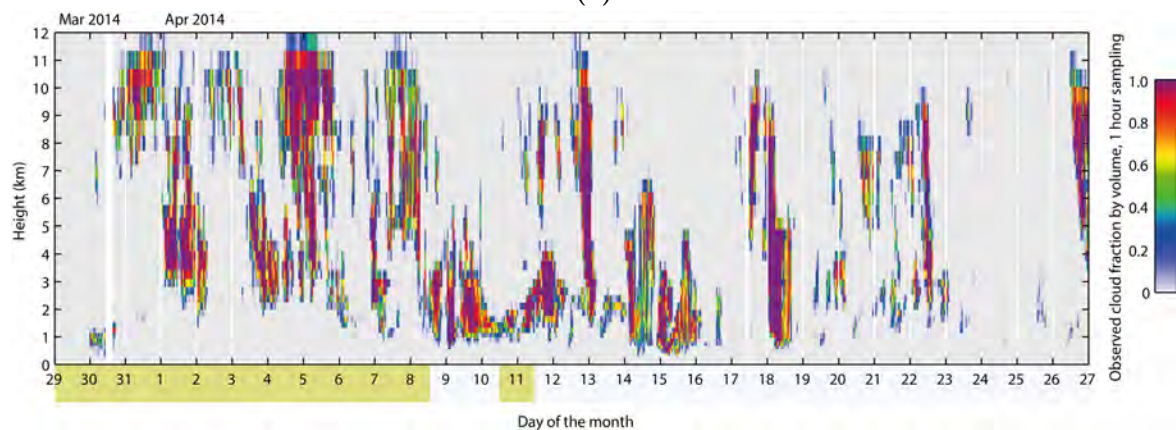
- Textor, C., M. Schulz, S. Guibert, S. Kinne, Y. Balkanski, S. Bauer, T. Berntsen, T. Berglen, O. Boucher, M. Chin, F. Dentener, T. Diehl, R. Easter, H. Feichter, D. Fillmore, S. Ghan, P. Ginoux, S. Gong, A. Grini, J. Hendricks, L. Horowitz, P. Huang, I. Isaksen, I. Iversen, S. Kloster, D. Koch, A. Kirkevåg, J. E. Kristjansson, M. Krol, A. Lauer, J. F. Lamarque, X. Liu, V. Montanaro, G. Myhre, J. Penner, G. Pitari, S. Reddy, Ø. Seland, P. Stier, T. Takemura, and X. Tie (2006), Analysis and quantification of the diversities of aerosol life cycles within AeroCom, *Atmospheric Chemistry & Physics*, *6*, 1777-1813.
- TROPOS (2016), TROPOS, <http://www.tropos.de/en/research/projects-infrastructures-technology/>.
- Twomey, S. (1974), Pollution and the planetary albedo, *Atmospheric Environment*, *8*, 1251-1256, doi:10.1016/0004-6981(74)90004-3.
- Twomey, S. (1977), The influence of pollution on the shortwave albedo of clouds., *Journal of Atmospheric Sciences*, *34*, 1149-1154, doi:10.1175/1520-0469(1977)034<1149:TIOPOP>2.0.CO;2.
- Twomey, S. A., M. Piepgrass, and T. L. Wolfe (1984), An assessment of the impact of pollution of global cloud albedo, *Tellus Series B Chemical and Physical Meteorology B*, *36*, 356, doi:10.1111/j.1600-0889.1984.tb00254.x.
- Vogel, B., H. Vogel, D. Bäumer, M. Bangert, K. Lundgren, R. Rinke, and T. Stanelle (2009), The comprehensive model system COSMO-ART - Radiative impact of aerosol on the state of the atmosphere on the regional scale, *Atmospheric Chemistry & Physics*, *9*, 8661-8680.
- Wandinger, U. (2012), Observation of aerosol-cloud-turbulence interaction with integrated remote-sensing instrumentation, *Proceedings 26th ILRC*.
- Weitkamp, C. (2005), *Lidar: Range-resolved optical remote sensing of the atmosphere*, Springer Series in Optical Sciences, Springer.
- Westbrook, C. D., and A. J. Illingworth (2011), Evidence that ice forms primarily in supercooled liquid clouds at temperatures $> -27^{\circ}\text{C}$, *Geophysical Research Letters*, *38*, L14808, doi:10.1029/2011GL048021.
- William Putman, N. (2016), Portrait of global aerosols, https://www.nasa.gov/sites/default/files/images/706644main_705852main_GEOS5_full_full.jpeg.
- Zender, C. S., R. L. Miller, and I. Tegen (2004), Quantifying mineral dust mass budgets: Terminology, constraints, and current estimates, *EOS Transactions*, *85*, 509-512, doi:10.1029/2004EO480002.
- Zhang, D., Z. Wang, A. Heymsfield, J. Fan, D. Liu, and M. Zhao (2012), Quantifying the impact of dust on heterogeneous ice generation in midlevel supercooled stratiform clouds, *Geophysical Research Letters*, *39*, L18805, doi:10.1029/2012GL052831.
-

Appendix A

Case study observations scaled on the COSMO-EU and COSMO-DE grid

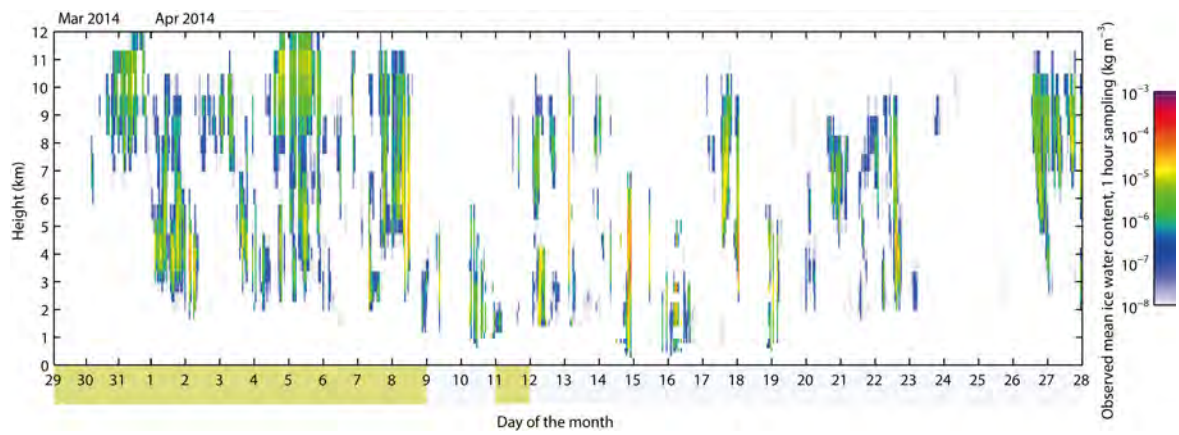


(a)

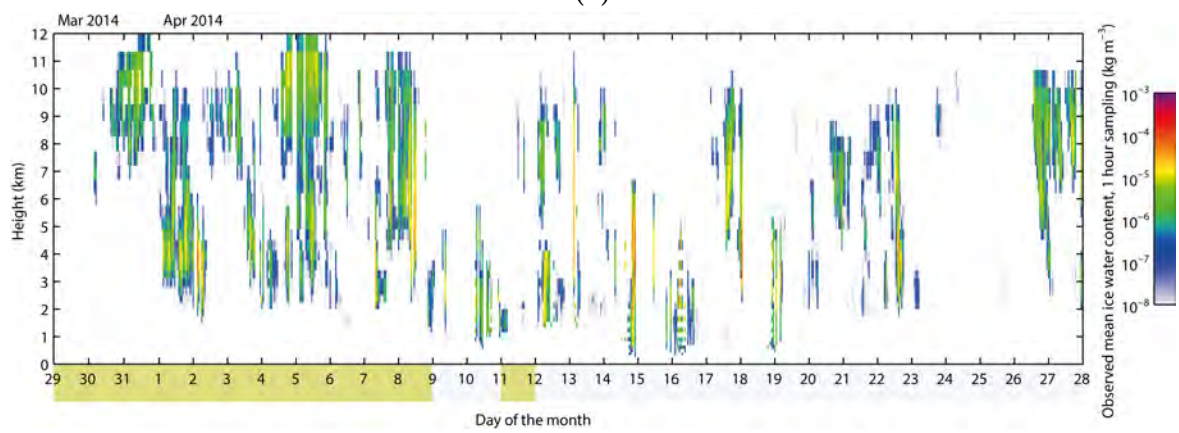


(b)

Figure A.1: (a) represents the cloud fraction observations in spring of 2014 scaled on the COSMO-EU grid. (b) shows the same scaled on the COSMO-DE grid.



(a)



(b)

Figure A.2: a) represents the IWC observations in spring of 2014 scaled on the COSMO-EU grid. (b) shows the same scaled on the COSMO-DE grid.

List of Figures

1.1	Development of the forecast skills of NWP models for the three-, five-, seven-, and ten-day forecasts on the northern hemisphere (NH, thick line) and on the southern hemisphere (SH, thin line) [Bauer <i>et al.</i> , 2015].	1
1.2	Portrait of the global aerosol distribution. Green indicates smoke rising from fires, white sulfate from volcanoes and fossil fuel emissions, blue sea salt inside cyclones, and red is dust erosion [William Putman, 2016].	2
2.1	Schematic visualization of mineral dust interaction with shortwave (SW) and longwave (LW) radiation during daytime [Choobari <i>et al.</i> , 2014]. SW ₁ indicates the incoming shortwave radiation at the top of atmosphere (TOA), and SW ₀ and LW ₀ the outgoing radiation at the surface.	6
2.2	Aerosol optical thickness (AOT) from smoke and dust (a) and only smoke (b) on the 31st of January 2008 at 550 nm wavelength [Heinold <i>et al.</i> , 2011b].	8
2.3	Instantaneous net radiative forcing induced by dust and smoke on the 31st of January 2008. The upper row shows the effect at noon (12:00 UTC), the lower at night (24:00 UTC). Left for the top of atmosphere (TOA), center for the surface and right for the atmosphere (TOA minus surface) [Heinold <i>et al.</i> , 2011b].	9
2.4	Illustration of the indirect aerosol effects. Adapted from Solomon <i>et al.</i> [2007].	11
2.5	Amount of ice in mixed-phase cloud in terms of the cloud top temperature and dust concentration (c_D). The black solid line marks the ratio at a high ($c_D \geq 2 \mu\text{g m}^{-3}$), the dashed line at a small dust concentration ($c_D < 0.001 \mu\text{g m}^{-3}$) and the grey line represents the whole data set [Seifert <i>et al.</i> , 2010].	12
2.6	Satellite observations of dust effects on mixed-phase clouds from Zhang <i>et al.</i> [2012]. For the three different regions (dusty, non-dusty and southern regions) the amount of ice (a), the maximum radar reflectivity factor Z_{e_max} (b) and the icw water path (IWP) (c) in MCCSs in terms of their CTT is represented.	13
2.7	Topological map with the domains D0, D1, and Ω [Bangert <i>et al.</i> , 2012].	14

2.8	2.8a represents the measured and simulated aerosol mass concentration, PM_{10} , between the 23rd and the 30th of May 2008. Black solid line for measurements at Hohenpeissenberg, Germany, grey solid line for simulation of domain D1 and shadings for simulation of domain D0. In Figure 2.8b the anomalies between simulated and measured temperature in area Ω for the period from 26th till 30th May are shown [Bangert et al., 2012].	15
2.9	Results for the domain D1 shown in Figure 2.7 adopted from Bangert et al. [2012]. Left column from top down: Aerosol optical thickness (τ), vertical velocity inside the clouds (w_{cloud}), liquid water path (LWP) and ice water path (IWP); right column from top down: radiant flux of shortwave radiation at surface (F_{sw}), radiative flux of longwave radiation at surface (F_{lw}), hourly precipitation rate (R_{1h}), and the 2-m temperature (T_{2m}). Solid lines represent simulations C (black) and CR (gray) while the dashed lines represent simulations REF (black) and R (grey).	16
3.1	Instrumentation of LACROS at TROPOS [TROPOS, 2016]. Used in this study is data from the cloud radar Mira-35 (1), the lidar ceilometer CHM 15kx (7) or the raman lidar Polly ^{XT} (8), and the microwave radiometer HATPRO [a].	18
3.2	Initially classification scheme for lidar backscatter and depolarization [Shupe, 2007].	23
3.3	Classification scheme for cloud radar reflectivity, Doppler velocity and spectrum. Left for $T > 0^\circ\text{C}$, center for $T < 0^\circ\text{C}$ and $W_D > 0.4 \text{ m s}^{-1}$, and right for $T < 0^\circ\text{C}$ and $W_D < 0.4 \text{ m s}^{-1}$ [Shupe, 2007].	24
3.4	Cloudnet measurements for the 05th of April 2014 at Leipzig [Cloudnet, 2016]. From top down: radar reflectivity factor, Doppler velocity, spectral width, and linear depolarization ratio measured with the cloud radar and particle backscatter coefficient at 1064 nm, and particle depolarization ratio at 532 nm measured with lidar as well as rain rate observed with a rain gauge, and liquid water path derived from the microwave radiometer measurements.	26
3.5	Cloudnet classification scheme for the measurements on the 05th of April 2014 at Leipzig shown in Figure 3.4 [Cloudnet, 2016]. (a) shows the resulting classification and (b) on which measurements the classification is based on.	27
3.6	IWC and LWC determined by Cloudnet for the 5th of April 2014 for Leipzig. (a) represents the IWC and (b) shows the correspondent scaled LWC.	28
6.1	Simulated dust concentration during outbreak over Leipzig in March and April 2014 [DREAM, 2015]	37

6.2	Observations and model results for the cloud fraction from the 29th of March until the 28th of April 2014. The top row represents the observations scaled on the ECMWF-IFS model grid. COSMO-EU, COSMO-DE, and ECMWF-IFS forecasts are plotted in the second, third and fourth row, respectively. Days classified as dust-laden are highlighted in ocher and low-dust days in light blue.	39
6.3	Observations and model results for the ice water content from the 29th of March until the 28th of April 2014. The top row represents the observations scaled on the ECMWF-IFS model grid. COSMO-EU, COSMO-DE, and ECMWF-IFS forecasts are plotted in the second, third and fourth row, respectively. Days classified as dust-laden are highlighted in ocher and low-dust days in light blue.	40
6.4	(a) represents the statistical analysis of the cloud fraction forecasts from COSMO-EU (left), COSMO-DE (middle) and ECMWF-IFS (right) during the low-dust (top, light blue) and dust-laden days (bottom, ocher). Observations are plotted in blue, while the model results minus undetectable ice clouds are depicted in red (the dashed line in the ECMWF-IFS analysis includes snow). In purple the unmodified model forecasts are represented. (b) shows the same for the IWC.	41
7.1	Maximum dust concentration during the analyzed time period from September 2011 until June 2014 for the different temperature regimes. The red line indicates the critical dust concentration $c_{D_{crit}} = 2 \mu\text{g m}^{-3}$, dust-laden days are indicated with a red star, dust-free days with a green one. Black stars identify days where no data was available. For the sake of clarity the lowest value of dust concentration in the plot has been set to $10^{-2} \mu\text{g m}^{-3}$	45
7.2	Long-term statistical analysis of cloud fraction forecast from COSMO-EU separated by dust concentration (horizontal) in certain temperature ranges (vertical).	46
7.3	Same as 7.2 but for COSMO-DE.	47
7.4	Long-term statistical analysis of ice water content forecast from COSMO-EU separated by dust concentration (horizontal) in certain temperature ranges (vertical).	48
7.5	Same as Figure 7.4 but for COSMO-DE.	49
7.6	Long-term statistical analysis of liquid water content forecast from COSMO-EU (top) and COSMO-DE (bottom) separated by dust concentration (horizontal) in certain temperature ranges (vertical).	50

8.1	Cloud-radar observation of the vertical velocity on 5 April 2014. (a) represents the vertical wind velocity on the 5th of May 2014 between 0:00 and 12:00 UTC. The alternating red and blue shadings indicate a strong mixing with a permanent change of the wind direction. (b) shows the histogram of the velocity of the vertical wind in 10 – 11 km height on the 5th of May 2014 between 2:00 and 5:00 UTC.	53
A.1	(a) represents the cloud fraction observations in spring of 2014 scaled on the COSMO-EU grid. (b) shows the same scaled on the COSMO-DE grid.	67
A.2	a) represents the IWC observations in spring of 2014 scaled on the COSMO-EU grid. (b) shows the same scaled on the COSMO-DE grid.	68

List of Tables

3.1	Approximated numbers of particles and diameter for liquid water, ice, rain and snow and the according values of Z_e calculated with equation 3.9.	22
5.1	Number of days during the long-term analysis that showed the corresponding dust concentration in the respective temperature range when cloud fraction data was available for COSMO-EU.	35

Acknowledgements

I would like to thank each and everyone who supported and motivated me in any kind during the process of this thesis.

First of all I would like to thank Prof. Dr. Ina Tegen and Jun.-Prof. Dr. Bernhard Pospichal for reviewing this t thesis.

A special thanks goes to Dr. Patric Seifert for his excellent supervision. He provided me all the necessary data, helped me with any question, and spend a lot of time with the proof-reading of this thesis. Thank you for all the support and all the effort you spend on this work.

I would like to thank the ground-based remote sensing group at TROPOS for all the coffee during the numerous coffee breaks and especially for providing me with the opportunity to present first results of this study at the DUST 2016 conference. Also I thank Bernd Heinold and Ina Tegen for their ideas and comments regarding my poster at the conference.

Even though it didn't work out within the designated time period for this thesis, I thank Bernd Heinold for doing his best to provide my the data from COSMO-MUSCAT.

And last, but not least, I would like to thank my friends, housemates and family for their support and the sometimes essential distraction.

Selbstständigkeitserklärung

Hiermit erkläre ich, dass ich die vorliegende Arbeit selbstständig verfasst habe und keinerlei außer den angegebenen Hilfsmitteln oder Quellen verwendet habe. Jegliche verwendete Literatur oder anderweitige Quelle wurde als solche gekennzeichnet und zitiert. Alle abgebildeten Grafiken, sofern sie nicht mit einem Quellenvermerk versehen sind, wurden von mir selbst erstellt. Des Weiteren wurde diese Arbeit noch nie in gleicher oder ähnlicher Form bei einer anderen Prüfungsbehörde eingereicht.

Ich erkläre mich damit einverstanden, eine positive Bewertung der Arbeit vorausgesetzt, dass Kopien dieser Arbeit in der Bücherei der Fakultät für Physik und Geowissenschaften der Universität Leipzig sowie am Leibniz Institut für Troposphärenforschung in Leipzig zur Verfügung gestellt werden.

Leipzig, July 22, 2016

Hannes Jascha Griesche
